

Uncertainty Analysis of Slug Calorimeters in the HyMETS Arc-Jet Facility

Chelsey C. Morrow* and Andrew J. Brune†
NASA Langley Research Center, Hampton, Virginia, 23681

The objective of this work is to perform an uncertainty analysis of the deduced stagnation heat flux environment on a slug calorimeter for conditions that span the performance envelope of the Hypersonic Materials Environmental Test System arc-jet facility located at NASA Langley Research Center. Analytical solutions are developed for boundary-value problems on the slug element accounting for non-ideal effects, including spatial variation in the slug heat flux, multi-dimensional thermal conduction, and back-face losses, which departs from the state-of-the-art method derived from the American Society of Testing and Materials. Boundary-value problem definitions are informed by preliminary finite element thermal analysis of the slug calorimeter assembly (including both slug and housing) and just the slug element. The analytical solutions are presented in a general sense and in a truncated form from error analysis. Results are shown in optimizing and validating the analytical models against available slug back-face thermal data. The optimization results indicate that the appropriate epistemic uncertainty of the deduced stagnation heat flux on the slug calorimeter is at most $\pm 2.5\%$ for both a high- and low-enthalpy test condition. In addition, a numerical approach is used to determine the aleatory (probabilistic) uncertainty component in the slug stagnation heat flux by applying a marching least-squares slope routine through the steady-state portion of the slug back-face thermal response. Results indicate a compromise between the number of samples and the filter frequency of slug back-face thermal data points when evaluating the standard deviation of the deduced stagnation heat flux statistics. When combining the mixed uncertainty, both aleatory and epistemic, the interval of uncertainty in the deduced stagnation heat flux is determined to be up to $\pm 4\%$, which is at least a 60% reduction from the standard uncertainty used in the state-of-the-art method.

Nomenclature

a_0	=	constant in 2D solution with variable heat flux
a_1	=	constant in 2D solution with variable heat flux
A_n	=	constant in steady-state series in the 2D solution with variable heat flux
B_n	=	constant in steady-state series in the 2D solution with variable heat flux
c	=	scale factor
C_p	=	specific heat of the slug, J/kg-K
C_{zn}	=	constant in variable heat flux transient solution with positive eigenvalues
E_z	=	constant in variable heat flux transient solution zero eigenvalue
f_L	=	slug back-face fractional heat flux loss
J_0	=	Bessel function of the first kind of order zero
J_1	=	Bessel function of the first kind of order one
L	=	length of slug, m
k	=	thermal conductivity of slug, W/m-K
m, n, z	=	set of positive integers 1, 2, 3, . . .
q_0	=	constant heat flux applied to the front face of slug, or constant in variable heat flux function $q(r)$, W/cm ²
q_1	=	constant in variable heat flux function $q(r)$, W/cm ³
q_2	=	constant in variable heat flux function $q(r)$, W/cm ⁴

*Doctoral Student, Department of Mathematics, North Dakota State University, Fargo, ND.

†Senior Aerospace Engineer, Structural and Thermal Systems Branch, Mail Stop 431, Senior Member AIAA.

$q(r)$	=	variable heat flux as a function of r , W/cm ²
q_{avg}	=	average heat flux value, W/cm ²
p	=	percent increase of the constant term q_0 at $r = r_0$
p_n	=	$\frac{\alpha_n}{r_0}$, eigenvalues for J_1
r	=	radial position from slug centerline at $r = 0$, m
r_0	=	radius of the slug, m
t	=	time, s
$T(x, t)$	=	temperature of a slug as a function of x and t , K
$T(r, x, t)$	=	temperature of a slug as a function of r, x , and t , K
$T_b(t)$	=	temperature of the back-face of the slug with respect to the time t , K
T_0	=	initial slug temperature at $t = 0$, K
T_r	=	the first partial derivative of the function T with respect to the variable r
T_{rr}	=	the second partial derivative of the function T with respect to the variable r
T_t	=	the first partial derivative of the function T with respect to the variable t
T_x	=	the first partial derivative of the function T with respect to the variable x
T_{xx}	=	the second partial derivative of the function T with respect to the variable x
$v(r, x, t)$	=	steady-state 2D solution with variable heat flux
v_z	=	$\frac{z\pi}{L}$, eigenvalues of sine function
$w(r, x, t)$	=	transient 2D solution with variable heat flux
x	=	position along length of slug from front face at $x = 0$, m
α	=	thermal diffusivity of slug, m ² /s
α_n	=	n th positive root of J_1
β^2	=	separation of variables constant for 2D steady-state solution
Δ	=	differential operator
ρ	=	density of the slug, kg/m ²

I. Introduction

Arc-jet test facilities are used to simulate heating and flow environments experienced in atmospheric entry and hypersonic flight. These test facilities are crucial for testing thermal protection materials and systems. Slug calorimeters are used for calibration of arc-jet test conditions in which heat losses from the slug to its holder are of concern as well as uncertainties associated with the slug calorimeter measurements. Brune et al. [1] performed a recent study on uncertainty quantification and validation as well as a sensitivity analysis of a high- and low-enthalpy test condition. Forty-seven sources of uncertainty were considered, such as instrumentation bias (including stagnation heat flux measurement) as well as surface catalysis input, chemical kinetic rates, and binary collision integrals in the computation fluid dynamics analysis (CFD) model. The calibration probe stagnation heat flux measurement bias was determined as a significant contributor in the uncertainty of stagnation heat flux computation.

Since 1996, NASA has used a simple, ideal approach involving a temperature slope of slug calorimeter data to evaluate the heat flux. However, this state-of-the-art method described in [2] uses the American Society of Testing and Materials (ASTM) standard E457-08 with a $\pm 10\%$ uncertainty on the calculated heat flux value. Other studies have attempted to address modeling of the slug heat flux probes in an effort to provide an analysis of the thermal environment and uncertainty, either through finite element or analytical methods. Hightower [3] presents two one-dimensional analytical models for a NASA Ames probe design - one with the assumption of no heat losses and constant physical properties and the other with assumptions of losses and variable heat capacity with temperature. Nawaz [4] discusses various methods for evaluating calorimeter measurements for a NASA Ames probe design, including Hightower, ASTM, and finite element analysis (FEA). Both Dalir [5] and Jain [6] present analytical models for higher dimensions with the assumption that the geometry of the slug calorimeter is a sphere. While each of these studies provides valuable information, they do not address methods that are specific to the NASA Langley Hypersonic Material Environment Test System (HyMETS) arc-jet facility for a flat-faced (cylindrical) slug geometry. Furthermore, these studies do not address some non-ideal effects, including spatial variation of heat sources in combination with thermal path losses.

The primary objective of this work is to characterize and reduce the uncertainty in the deduced heat flux of the flat-faced slug calorimeter in the HyMETS arc-jet facility. Analytical models are developed to incorporate a combination of non-ideal effects, including factors related to spatially varying heat flux on, and heat losses from, the flat-faced slug element. These analytical models are then validated and optimized against back-face slug temperature data from a low-

and high-enthalpy test condition. Using the results of the optimization, a new range for both epistemic (bias) uncertainty in the deduced stagnation heat flux on the slug element can be determined. A second component of the uncertainty (aleatory) is also evaluated with a numerical approach in quantifying the local temperature slopes, marching through time, in the steady-state portion of the slug back-face temperature data from each test condition. In the end, a mixed uncertainty assessment is provided given the analysis performed in this study, which can be used in future studies for model validation and calibration with CFD.

This paper is organized to first present an overview of the HyMETS facility configuration and instrumentation in Section II. Section III presents the initial-boundary value problems that incorporate non-ideal effects, informed by preliminary high-fidelity slug probe thermal analysis, and the developed analytical solution approaches. In Section IV, an evaluation of the epistemic uncertainty in the deduced stagnation heat flux of the slug calorimeter is performed based on the results of optimizing analytical solutions against available slug thermal data from the HyMETS arc-jet facility at low- and high-enthalpy test conditions. In addition, the aleatory uncertainty is evaluated using a least-squares fit marching routine to generate statistics in the temporal variation of the deduced stagnation heat flux. The results of the two components of uncertainty will be compiled into a probability box plot and compared against the uncertainty used in Brune et al. [1], which is based on the state-of-the-art ASTM standard procedure. Conclusions of this work are provided in Section V.

II. Test Facility Details

Arc-jet facilities are typically used to develop and demonstrate high-temperature materials at flight-relevant heat flux, surface pressure, and shear force environments. In this study, the HyMETS facility at NASA Langley Research Center is considered to assess and characterize the uncertainty of the slug calorimeter specifically used at two arc heater conditions that span the facility’s performance envelope. The history of the facility use can be found in the work by Splinter et al. [7], most of which includes material characterization for hypersonic vehicles [8–10].

The HyMETS facility uses a segmented-constrictor dc-electric arc heater with injected discrete test gases to form mixtures of diatomic nitrogen, diatomic oxygen, and argon. The segmented arc heater column along with power supply and water lines is shown in Figures 1 and 2. The arc heater is mounted on the outside of the test cabin door. The heater consists of water-cooled components, which include a copper cathode with tungsten button emitter, electrically-isolated copper segment constrictors with a 1.27-cm diameter bore, and a copper divergent-ring anode. Test gasses are injected tangentially into the bore of the arc heater generator at six discrete locations and can be mixed at various levels to desired atmospheric composition. The gases are heated by a high-voltage electric arc that is maintained between the cathode and anode to create a high-temperature dissociated gas via radiation and gas conduction modes. The HyMETS facility has several viewports to obtain video and pyrometer thermal data of the test specimen and are located on the test cabin door and test cabin walls. A detailed description and overview of the HyMETS facility and performance envelopes for stagnation testing can be found in the literature [7, 11].

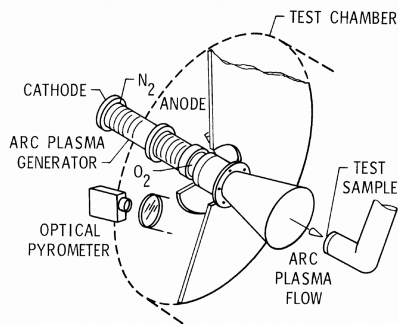


Fig. 1 HyMETS test setup schematic.

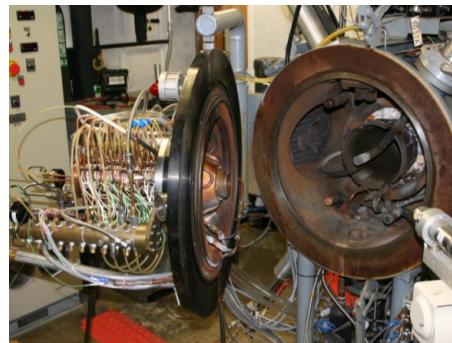


Fig. 2 HyMETS facility test setup.

For stagnation testing, a water-cooled 6.35-cm exit diameter conical nozzle with a 1.27-cm throat diameter and half angle of 12 degrees, made of copper and attached to the arc heater system, is used to provide the appropriate freestream conditions for a combination of desired heat flux and pressure at the probe surface. The high-temperature flow from the

arc heater is accelerated through the nozzle and exhausted into a 60.9-cm wide by 91.4-cm long vacuum test cabin. The flow proceeds downstream of the test cabin into a collector cone, a 15.24-cm diameter constant cross-section diffuser, and a coiled-copper tubing heat exchanger to decelerate and cool the flow. The test cabin is pumped to the desired conditions with a mechanical pumping system. Test models are positioned on the centerline of the flow just downstream of the nozzle exit. A Pitot probe, a slug calorimeter, and a TPS specimen are injected in sequential order into the flow during each run.

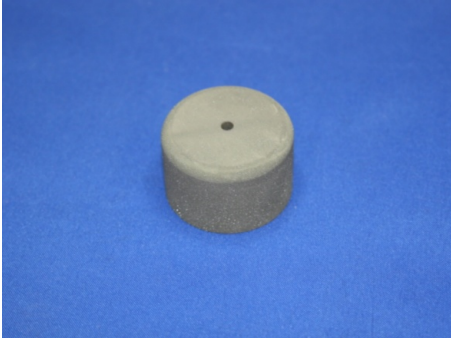


Fig. 3 Pitot tube.



Fig. 4 Copper slug calorimeter.

A flat-face Pitot probe and copper slug calorimeter [12, 13] shown in Figures 3 and 4 respectively, are used to determine the stagnation surface pressure and heat flux during each run. The copper slug calorimeter is used to determine the cold-wall heat flux and consists of an un-cooled slug sensor element that is 1.27-cm diameter by 1.27-cm long with an uncooled shroud that is 3.3-cm diameter by 2.16-cm long and a flow-face edge radius of 0.318 centimeters. The slug sensor element and shroud are fabricated out of oxygen-free high-conductivity copper. The slug sensor element has a 0.005-cm wide “insulating” air gap between it and the shroud and is held in place using six cone-tipped set-screws. The slug sensor element also has a Type-K thermocouple mounted on its back surface to measure temperature rise. The length, diameter, and mass of the slug sensor element are measured prior to calorimeter assembly. The copper slug calorimeter is inserted into a steady-state flow for up to five seconds so that it achieves a back-face temperature rise of several hundred degrees Fahrenheit, not to exceed a final temperature of 588 K (600°F). The state-of-the-art method is based on the ASTM standard procedure for deducing the heat flux [12]. The heat flux is deduced from the density of the copper slug sensor element ρ , the specific heat capacity of the element C_p , the length of the element L , and the slope of the temperature rise $\Delta T/\Delta t$ from the linear portion of the temperature response curve, measured by the back-face Type-K thermocouple, using Equation 1 :

$$\dot{q}_w = \rho C_p L \left(\frac{\Delta T}{\Delta t} \right) \quad (1)$$

The uncertainty of the resulting method given by Eq. 1 is assumed to be $\pm 10\%$ [7, 13]. In this study, two test conditions are considered, ranging in low to high enthalpy, with sufficient detail described and presented in Brune et al. [1]. The low enthalpy condition is defined throughout the paper with a reported stagnation heat flux reference of 56.7 W/cm², using the above ASTM approach. The high enthalpy condition is defined throughout the paper with a reported stagnation heat flux reference of 243.1 W/cm², using the above ASTM approach. The ASTM method is described in this paper interchangeably as the state-of-the-art method.

III. Modeling Approach of Slug Calorimeter Temperature Environments

In the previous section, details of the NASA Langley HyMETS arc-jet test facility were presented along with the state-of-the-art ASTM method and reference test conditions. In this section, analytical solutions are developed for boundary-value problems on the slug element accounting for non-ideal effects, including spatial variation in the slug heat flux, multi-dimensional thermal conduction, and back-face losses, which departs from the state-of-the-art method. In Section III.A, the boundary-value problem definitions are informed by preliminary finite element thermal analysis of

the slug calorimeter assembly (including both slug and housing) and just the slug element. In Sections III.B.1 - III.B.3, the analytical solutions are presented in a general sense with the derived boundary value problems on the slug element. Sections III.C.1 - III.C.2 present truncation analysis to simplify the complex solutions while maintaining accuracy.

A. Preliminary Finite Element Analysis (FEA)

A three-dimensional finite element model of the slug calorimeter (Figure 5a), is developed in COMSOL to analyze the non-ideal thermal effects, including radiation and conduction losses and spatial (radial) variation of a heat flux source (as opposed to the ideal constant heat flux source). A simplified slug element model (Figure 5b) is also developed to compare against the higher-fidelity slug calorimeter model. Figure 6 shows a schematic of the various components of the slug calorimeter, including the slug element, housing, and a copper sting mount with a hole to route a Type-K thermocouple from the slug back-face to connectors. The copper sting mount has a potential air gap, when installed, and could be in contact with a significant portion of the slug back-face area, with exception of the thermocouple drill hole aligned with at the centerline of the slug back face. In either case (with or without contact), there is the potential for conduction or radiation loss from the slug. In addition, studies have shown that the spatial variation of the heat flux can be significant, especially for slug calorimeters with small base diameters [1, 14], which can potentially impact the thermal response of the slug element.



(a) Slug Calorimeter Model (with Housing).

(b) Slug Element Only Model (No Housing).

Fig. 5 CAD model geometries implemented in the preliminary finite element analysis.

In this preliminary analysis, constant material properties are taken from sources, including the National Institute of Standards and Technology (NIST) Reference Database [15–17]. Although the thermal properties are presented as temperature-dependent in these references, the slug calorimeters are subjected to limited exposure time and temperature range in the flow between 285 and 400 Kelvin. Constant material properties are set to approximate room temperature values with a thermal conductivity of 400 W/m-K and specific heat of 385.2 J/kg-K. The density of copper is set to the average of five slug elements at 8821 kg/m³. The material property values deviate by no more than 1-2% in the applicable temperature range of data in which the slug calorimeter is in the flow. The set screws are treated as alloy steel with default material property values in COMSOL [18].

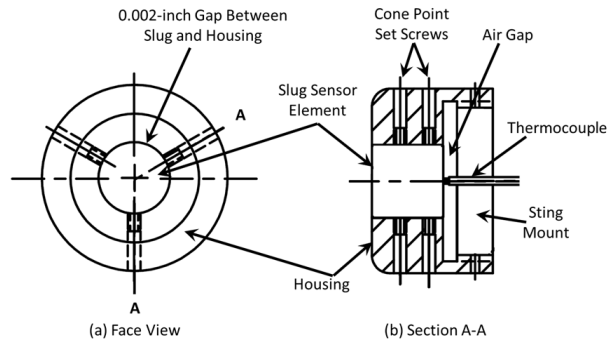


Fig. 6 Schematic of slug calorimeter.

The preliminary simulations of the slug calorimeter model implement internal radiation between the slug element

and housing with an emissivity of polished copper of 0.05. The slug element is modeled in perfect contact with the sting mount as a bounding case of a potential air gap. Constant heat flux is applied to the external surfaces of the slug and holder based on the reported heat flux at the high enthalpy condition. The spatial heat flux distribution is applied based on CFD data from Brune et al. [1]. Note that the heat fluxes are applied as cold-wall values (low temperature environment and limited exposure time). With emissivity values of polished copper between 0.02 and 0.07 and tested copper with a thick oxide layer of 0.78, radiation cooling of the copper slug to test cabin walls and vacuum environment is considered negligible with a magnitude less than 1% of the convective heat flux magnitude. Thermal expansion and convective flow in the gap between the holder and slug element are also considered negligible due to limited time of exposure in the arc flow. For the simplified slug element model, the sides of the slug are modeled as adiabatic (no heat transfer loss). Constant and spatially-varying heat fluxes are applied to the front surface of the slug element, consistent with those applied to the slug calorimeter model. A constant conduction loss heat flux source is modeled on the back face of the slug as a percentage of the front-face heat flux.

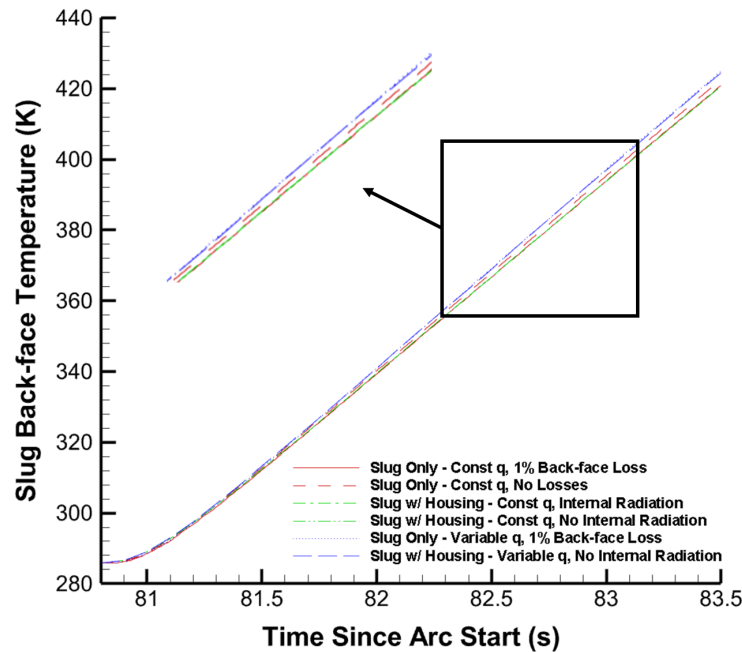


Fig. 7 FEA results comparing back-face temperature predictions for various non-ideal effects with the slug element model and full slug calorimeter assembly.

Figure 7 presents the thermal response as a function of arc run time of the slug at the center of the back face, corresponding to the location where the thermocouple bead is placed for a temperature measurement. Results are shown for slug calorimeter (slug w/ housing) model with and without internal radiation for both constant and spatially-varying heat flux distributions on the external surfaces. The thermal response of the slug element (slug only) model with and without losses for both constant and spatially-varying heat flux sources are compared to those of the slug calorimeter model. Looking at the slug calorimeter model results in green, the internal radiation has no impact to the back-face temperature response of the slug. When considering the slug element model results (red lines) for the constant heat flux case, the conduction losses to the copper sting mount aft of the slug have a noticeable impact in the back-face steady-state slug temperature slope, and the temperature response of the slug with a back-face loss of 1% of the front face heat flux agrees with the higher-fidelity slug calorimeter model. The results shown in blue also indicate a more significant impact to the steady-state temperature slope due to spatial variations in the front face heat flux distribution. In following subsections, analytical solutions will be developed for the simplified slug model with appropriate boundary value problems based on the significant non-ideal thermal effects, including back-face slug conduction losses and spatial (radial) variation of the front-face heat flux on the slug. The multi-dimensionality of the copper conduction will also be considered in the development of these analytical solutions.

B. Analytical Solutions

1. Constant Heat Flux without Radial Conduction

Consider a one-dimensional approach with assumed heat losses on the back-face of the slug with constant heat flux q_0 and constant properties. This gives the standard governing equation

$$T_{xx} = \frac{1}{\alpha} T_t \quad (2)$$

where $T_{xx} = \frac{\partial^2 T}{\partial x^2}$, $T_t = \frac{\partial T}{\partial t}$, and α is constant. The boundary and initial conditions informed by FEA are

$$T_x(0, t) = -\frac{q_0}{k} \quad T_x(L, t) = -f_L \left(\frac{q_0}{k} \right) \quad T(x, 0) = T_0 \quad (3)$$

where T_0 represents the initial constant uniform temperature of the slug calorimeter, k is the thermal conductivity constant, and f_L is the fractional loss. A schematic of the boundary value problem is provided in Figure 8 .

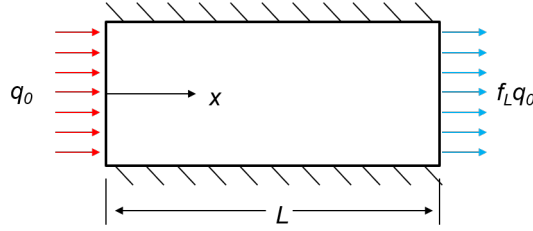


Fig. 8 Boundary conditions for constant heat flux with one-dimensional conduction.

This initial-value problem is very similar to the one proposed by Hightower et al. [3] in which the method of separation of variables is used to find a solution of the form $T(x, t) = (\text{steady state}) + (\text{transient state})$. Using the same approach, the general solution is

$$T(x, t) = T_0 + \frac{(1 - f_L)q_0}{2kL} x^2 - \frac{q_0}{k} x + \frac{(2 + f_L)q_0 L}{6k} + \frac{(1 - f_L)\alpha q_0 t}{kL} + \frac{2q_0 L}{k\pi^2} \sum_{n=1}^{\infty} \left[\frac{(-1)^n f_L - 1}{n^2} \right] e^{-\alpha \left(\frac{n\pi}{L} \right)^2 t} \cos \left(\frac{n\pi x}{L} \right) \quad (4)$$

More details on the derivation and verification of Eqn. 4 are provided in the Appendix. The back-face temperature of the slug that satisfies the initial-boundary value problem is $T_b(t) = T(L, t)$:

$$T_b(t) = T_0 - \frac{(1 + 2f_L)q_0 L}{6k} + \frac{(1 - f_L)\alpha q_0 t}{kL} + \frac{2q_0 L}{k\pi^2} \sum_{n=1}^{\infty} \left[\frac{(-1)^{n+1} + f_L}{n^2} \right] e^{-\alpha \left(\frac{n\pi}{L} \right)^2 t} \quad (5)$$

A two-dimensional approach with assumed heat losses on the back-face of the slug with radial conduction, constant heat flux q_0 , and constant properties is also considered. The resulting analytical solution, $T(r, x, t)$, does not depend on the variable r (distance from the center of the slug) and therefore reduces to Eqn. 4 . The derivation and verification for these boundary conditions on the slug element are provided in the Appendix.

2. Variable Heat Flux without Radial Conduction

Now assume heat flux is no longer constant, but spatially varying in the radial direction. Based on an empirical fit of heat flux data from the CFD analysis, the heat flux follows a quadratic form. That is, $q(r)$ is of the form $q(r) = q_2 r^2 + q_1 r + q_0$ for some constants q_2 , q_1 , and q_0 . Note that q_0 here represents the stagnation heat flux at $r = 0$ and is different from that defined in the previous subsection as a constant heat flux. The average value of $q(r)$ is

$$q_{avg} = \frac{1}{\pi(r_0)^2} \int_0^{2\pi} \int_0^{r_0} r q(r) dr d\theta = \frac{q_2(r_0)^2}{2} + \frac{2q_1 r_0}{3} + q_0 \quad (6)$$

where r_0 is the radius of the slug. This equation gives a formula for q_0 in terms of q_2 , q_1 , and q_{avg} :

$$q_0 = q_{avg} - \frac{q_2(r_0)^2}{2} - \frac{2q_1r_0}{3}. \quad (7)$$

Imposing the initial conditions $q'(0) = 0$ and $q(r_0) = pq_0$, where p is the percent increase of the constant term q_0 , gives the values of q_1 and q_2 to be

$$q_1 = 0 \quad q_2 = \frac{2(p-1)q_{avg}}{(r_0)^2(1+p)}. \quad (8)$$

Given specified values of p and q_{avg} , the coefficients of the quadratic heat flux, q_2 , q_1 , and q_0 , can be computed using Eqns. 7 and 8. This simple computation allows Eqn. 4 to be adjusted to accommodate spatial variation in heat flux. In particular, replacing q_0 in Eqn. 4 with the given q_{avg} value adjusts the general solution to

$$T(x, t) = T_0 + \frac{(1-f_L)q_{avg}}{2kL}x^2 - \frac{q_{avg}}{k}x + \frac{(2+f_L)q_{avg}L}{6k} + \frac{(1-f_L)\alpha q_{avg}t}{kL} + \frac{2q_{avg}L}{k\pi^2} \sum_{n=1}^{\infty} \left[\frac{(-1)^n f_L - 1}{n^2} \right] e^{-\alpha \left(\frac{n\pi}{L}\right)^2 t} \cos\left(\frac{n\pi x}{L}\right) \quad (9)$$

The above model satisfies the one-dimensional boundary value problem. Therefore, the back-face temperature of the slug then becomes

$$T_b(t) = T_0 - \frac{(1+2f_L)q_{avg}L}{6k} + \frac{(1-f_L)\alpha q_{avg}t}{kL} + \frac{2q_{avg}L}{k\pi^2} \sum_{n=1}^{\infty} \left[\frac{(-1)^{n+1} + f_L}{n^2} \right] e^{-\alpha \left(\frac{n\pi}{L}\right)^2 t} \quad (10)$$

3. Variable Heat Flux With Radial Conduction

Consider a two-dimensional approach with the assumption of variable heat flux $q(r) = q_2r^2 + q_1r + q_0$. This gives the governing equation

$$T_{xx} + T_{rr} = \frac{1}{\alpha}T_t - \frac{1}{r}T_r \quad (11)$$

with initial condition $T(r, x, 0) = T_0$ and boundary conditions

$$T_r(0, x, t) = 0 \quad T_r(r_0, x, t) = 0 \quad (12)$$

$$T_x(r, 0, t) = -\frac{q(r)}{k} \quad T_x(r, L, t) = -f_L \left(\frac{q(r)}{k} \right) \quad (13)$$

where r_0 is the radius of the slug. A schematic of the boundary value problem is provided in Figure 9.

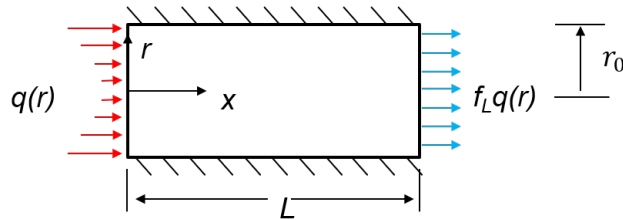


Fig. 9 Boundary conditions for variable heat flux with two-dimensional conduction.

Similar to the one-dimensional approach, assume the solution is of the form

$$T(r, x, t) = (\text{steady state}) + (\text{transient}) = v(r, x, t) + w(r, x, t) \quad (14)$$

Two analytical solutions of this form exist, and they depend on the choice of eigenvalues in the transient solution, $w(r, x, t)$. Using the separation of variables $w(r, x, t) = R(r)X(x)\tau(t)$, the eigenvalues of $R(r)$ are associated to the roots of the Bessel function J_1 .

In the case of positive roots of J_1 , α_n , where n is a positive integer, gives the eigenvalues for $R(r)$ to be $p_n = \frac{\alpha_n}{r_0}$ for all positive integers n . The general solution is

$$T(r, x, t) = T_0 + \alpha\beta^2 t + \frac{\beta^2}{2}x^2 + a_1x + a_0 + \sum_{n=1}^{\infty} [A_n \cosh(p_n x) + B_n \sinh(p_n x)] J_0(p_n r) + \sum_{n=1}^{\infty} \sum_{z=1}^{\infty} C_{zn} e^{-(v_z^2 + p_n^2)at} \cos(v_z x) J_0(p_n r) \quad (15)$$

where $A_n, B_n, C_{zn}, \beta^2, a_1, a_0$ are constants and $v_z = \frac{z\pi}{L}$ for all positive integers z .

In the case of zero as the root of J_1 , the associated eigenvalues of $R(r)$ are zero. This yields the general solution as

$$T(r, x, t) = T_0 + \alpha\beta^2 t + \frac{\beta^2}{2}x^2 + a_1x + a_0 + \sum_{n=1}^{\infty} [A_n \cosh(p_n x) + B_n \sinh(p_n x)] J_0(p_n r) + \sum_{z=1}^{\infty} E_z e^{-v_z^2 at} \cos(v_z x) \quad (16)$$

where $A_n, B_n, E_z, \beta^2, a_1, a_0$ are constants.

The coefficients of x^2, x , and t are β^2, a_1 , and a_0 , respectively. The values of these constants are

$$\beta^2 = \frac{(1 - f_L)q_{avg}}{kL} \quad a_1 = -\frac{q_{avg}}{k} \quad a_0 = \frac{(2 + f_L)q_{avg}L}{6k} \quad (17)$$

The Appendix contains the process used to calculate the value of β^2 and also provides justification that a_0 and a_1 can be arbitrary. Thus, the values of a_0 and a_1 are chosen so that they are comparable to the corresponding terms in Eqn. 9.

Futhermore, using Fourier series and integration, the values of the remaining unknown constants in Eqns. 15 and 16 are as follows:

$$A_n = B_n \left[\frac{f_L - \cosh(p_n L)}{\sinh(p_n L)} \right] = B_n D_n \quad (18)$$

$$B_n = \frac{-2}{k p_n [J_0(\alpha_n)]^2} \sum_{m=1}^{\infty} \frac{(-1)^{m-1} (\alpha_n)^{2m-2}}{2^{2m-2} [(m-1)!]^2} \left[\frac{q_2(r_0)^2}{2m+2} + \frac{q_1 r_0}{2m+1} \right] \quad (19)$$

$$C_{zn} = \sum_{m=1}^{\infty} \frac{[(-1)^z f_L - 1]}{kL(p_n^2 + v_z^2)[J_0(\alpha_n)]^2} \left[\frac{(-1)^{m-1} (\alpha_n)^{2m-2}}{2^{2m-4} [(m-1)!]^2} \right] \left[\frac{q_2(r_0)^2}{2m+2} + \frac{q_1 r_0}{2m+1} \right] \quad (20)$$

$$E_z = \frac{(-1)^{z+1} (2\beta^2 L + 2a_1) + 2a_1}{L v_z^2} + \sum_{n=1}^{\infty} \sum_{m=1}^{\infty} \frac{[(-1)^z f_L - 1]}{kL(p_n^2 + v_z^2)[J_0(\alpha_n)]^2} \left[\frac{(-1)^{m-1} (\alpha_n)^{2m-2}}{2^{2m-4} [(m-1)!]^2} \right] \left[\frac{q_2(r_0)^2}{2m+2} + \frac{q_1 r_0}{2m+1} \right] \quad (21)$$

Evaluating Eqns. 15 and 16 at $x = L$ and $r = 0$ yields two models for the back-face centerline temperature of the slug. The positive eigenvalue solution is

$$T_b(t) = T_0 + \alpha\beta^2 t + \frac{\beta^2}{2}L^2 + a_1L + a_0 + \sum_{n=1}^{\infty} B_n D_n + \sum_{n=1}^{\infty} \sum_{z=1}^{\infty} (-1)^z C_{zn} e^{-(v_z^2 + p_n^2)at} \quad (22)$$

and the zero eigenvalue solution is

$$T_b(t) = T_0 + \alpha\beta^2 t + \frac{\beta^2}{2}L^2 + a_1L + a_0 + \sum_{n=1}^{\infty} B_n D_n + \sum_{z=1}^{\infty} (-1)^z E_z e^{-v_z^2 at}. \quad (23)$$

Both of these solutions satisfy the proposed initial-boundary value problem detailed in Eqns. 11, 12 and 13. The next section will present results showing that one of the above solutions is not valid and does not agree with the slug back-face temperature data. The Appendix provides details on the derivation and verification of the above solutions.

C. Truncation Analysis

Now that the analytical models for the back-face temperature have been established, it is necessary to determine the number of terms needed to approximate each infinite series in Eqns. 5, 10, 22, and 23 with reasonable accuracy. In order to accomplish this, it is necessary to set values for the quantities T_0 , q_2 , q_1 , and q_0 . The value for the initial temperature in the high-enthalpy condition is $T_0 = 285.93$ K, which is based on the mean temperature near $t = 0$ of slug calorimeter data. The values used for q_2 , q_1 , and q_0 are determined from an empirical fit of CFD data. In the high-enthalpy condition, these values are determined to be $q_2 = 45.5$ W/cm⁴, $q_1 = -2.5$ W/cm³, and $q_0 = 243.1$ W/cm². The thermal diffusivity, $\alpha = 0.00011773$ m²/s, and thermal conductivity, $k = 400$ W/m K, constants outlined in Section III.A as well as the length, $L = 0.0127$ m, and radius, $r_0 = 0.00635$ m, of the slug are also used in the truncation analysis. Furthermore, f_L is assigned the value of 0.01 per the preliminary analysis in Section III.A, which indicates a 1% conductive heat loss at the slug back-face.

1. Analytical 1D Conduction

The only series term in Eqn. 5 is the transient solution:

$$\frac{2q_0L}{k\pi^2} \sum_{n=1}^{\infty} \left[\frac{(-1)^{n+1} + f_L}{n^2} \right] e^{-\alpha \left(\frac{n\pi}{L}\right)^2 t}. \quad (24)$$

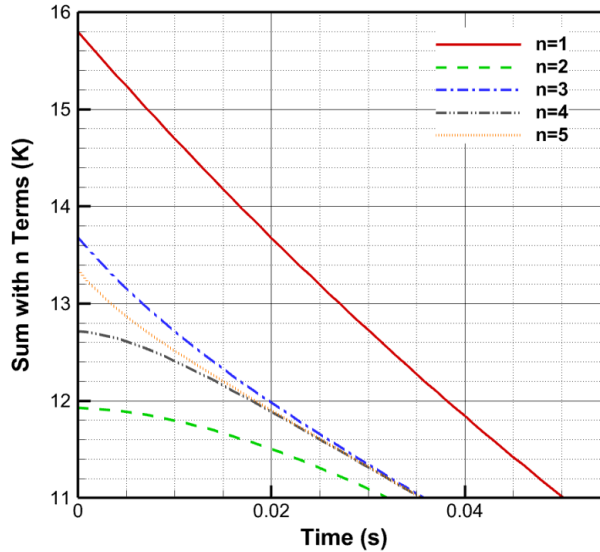


Fig. 10 Transient solution of Eqn. 4, summed up to the nth term.

Figure 10 shows the sum of the first five terms with the values of q_0 , k , L and f_L as indicated above. Note that the vertical axis is in units of degrees Kelvin. When $n = 3$, the sum is less than one Kelvin from the summation of terms greater than three. Thus, the transient solution in Eqn. 5 can be truncated to three terms. This truncation then simplifies the back-face temperature of the slug with constant heat flux (with or without radial conduction) as

$$T_b(t) = T_0 - \frac{(1 + 2f_L)q_0L}{6k} + \frac{(1 - f_L)\alpha q_0 t}{kL} + \frac{2q_0L}{k\pi^2} \left[(1 + f_L)e^{-\alpha \left(\frac{\pi}{L}\right)^2 t} - \frac{(1 - f_L)}{4}e^{-\alpha \left(\frac{2\pi}{L}\right)^2 t} + \frac{(1 + f_L)}{9}e^{-\alpha \left(\frac{3\pi}{L}\right)^2 t} \right]. \quad (25)$$

Since Eqn. 10 is an adjustment of Eqn. 5, the transient series can be truncated similarly. Therefore, Eqn. 10 can be truncated to three terms giving the simplified model:

$$T_b(t) = T_0 - \frac{(1 + 2f_L)q_{avg}L}{6k} + \frac{(1 - f_L)\alpha q_{avg} t}{kL} + \frac{2q_{avg}L}{k\pi^2} \left[(1 + f_L)e^{-\alpha \left(\frac{\pi}{L}\right)^2 t} - \frac{(1 - f_L)}{4}e^{-\alpha \left(\frac{2\pi}{L}\right)^2 t} + \frac{(1 + f_L)}{9}e^{-\alpha \left(\frac{3\pi}{L}\right)^2 t} \right]. \quad (26)$$

2. Analytical 2D Conduction

Compared to the solutions in the previous subsection, the analytical models in Eqns. 22 and 23 only differ in their transient solutions. Conveniently, the series in the transient solution of both models follows a similar pattern with similar conclusions. Therefore, this section will only highlight details of the the truncation analyses for solution in Eqn. 23, which is presented in Section III.B.3.

Eqn. 23 has series in both the steady-state solution and the transient solution. First, note that the steady-state series in Eqn. 18 is independent of time. Second, recall B_n contains an infinite sum with respect to the index m . Therefore, $\sum_{n=1}^{\infty} B_n D_n$ is a double sum in the indices n and m . Figure 11 shows the sum of the steady-state series for $1 \leq n \leq 5$ and $1 \leq m \leq 20$, which again uses the values of k, L, q_2 , and q_1 laid out in the introduction of this subsection. To summarize, if $n = 1, 2, 3, \dots, \epsilon$ for some fixed positive integer ϵ , then there is a sufficiently large positive integer m in which the sum is negligible. It should be noted that as ϵ increases, the number of m terms needed to make the sum negligible will also increase. Therefore, this series can be dropped from the steady-state solution in Eqn. 23.

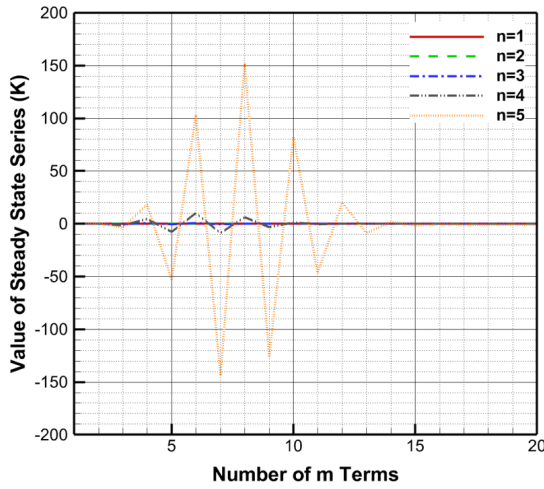


Fig. 11 Summation of steady-state series in Eqns. 22 and 23.

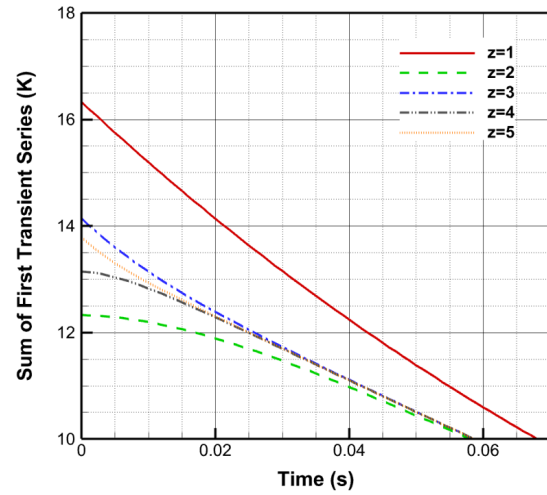


Fig. 12 Summation of first transient series in Eqn. 23.

The transient solution of Eqn. 23 has two infinite series:

$$\sum_{z=1}^{\infty} \left[\frac{(-1)^z 2a_1 - 2\beta^2 L - 2a_1}{Lv_z^2} \right] e^{-v_z^2 at} + \sum_{z=1}^{\infty} \sum_{n=1}^{\infty} \sum_{m=1}^{\infty} \frac{[(-1)^{z+1} + f_L]}{kL(p_n^2 + v_z^2)[J_0(\alpha_n)]^2} \left[\frac{(-1)^{m-1} (\alpha_n)^{2m-2}}{2^{2m-4} [(m-1)!]^2} \right] \left[\frac{q_2(r_0)^2}{2m+2} + \frac{q_1 r_0}{2m+1} \right] e^{-v_z^2 at} \quad (27)$$

The sum of the first transient series for up to the first five terms is shown in Figure 12. Since this mimics the pattern shown in Figure 10, the same conclusion of truncating the first transient series to three terms would provide a reasonable approximation.

Since the transient solution tends to zero as t increases, it is sufficient to evaluate Eqn. 23 at values near $t = 0$ in order to truncate the second transient series. Define $T_{znm}(t)$ to be Eqn. 23 with the suggested number of terms for the first transient series, along with the sum of all terms of the second transient solution from one to the specified values of z, n , and m . Figures 13 and 14 show the value of $T_{znm}(t)$, in units of Kelvin, at $t = 0$ and $t = 0.1$ seconds from the penetration time where $1 \leq z = n \leq 3$ and $1 \leq m \leq 11$. Observe that $T_{111}(t)$ is within one Kelvin of the value $T_{znm}(t)$ converges to for a fixed time t . The same holds true for all t when z, n , and m get large, even in the case when $z \neq n$. Therefore, the second transient series can be truncated to one term.

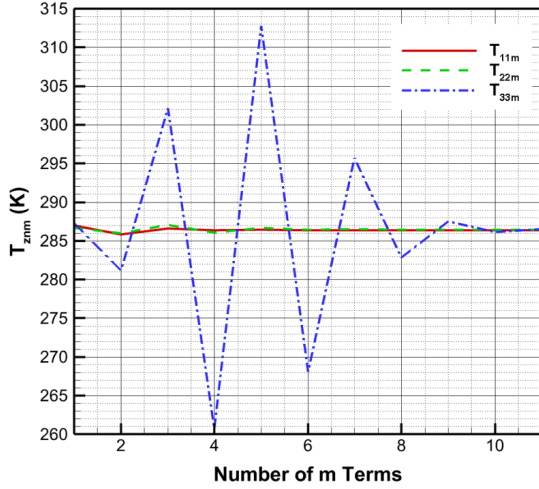


Fig. 13 Summation of second transient series in Eqn. 23 at $t=0$.

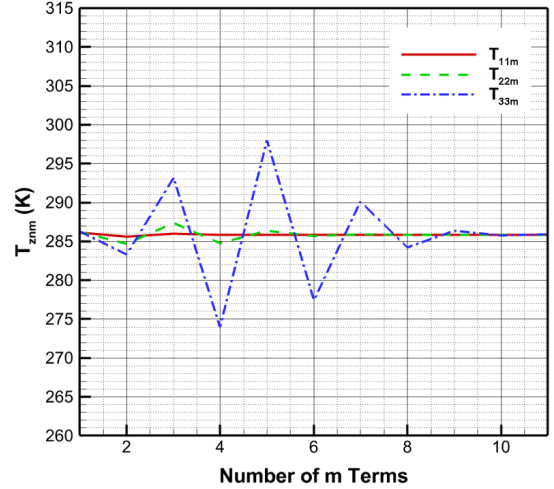


Fig. 14 Summation of second transient series of Eqn. 23 at $t=0.1$.

In conclusion, the steady-state series is negligible, the first transient series can be truncated to three terms, and the second transient series can be truncated to one term. Thus, Eqn. 23 can be reduced to

$$T_b(t) = T_0 + \alpha\beta^2 t + \frac{\beta^2}{2} L^2 + a_1 L + a_0 + \left[\frac{4.04}{kL[J_0(\alpha_1)]^2(p_1^2 + v_1^2)} \left[\frac{q_2 r_0^2}{4} + \frac{q_1 r_0}{3} \right] - \frac{4a_1 + 2\beta^2 L}{L \left(\frac{\pi}{L}\right)^2} \right] e^{-\left(\frac{\pi}{L}\right)^2 \alpha t} - \left(\frac{2\beta^2}{\left(\frac{2\pi}{L}\right)^2} \right) e^{-\left(\frac{2\pi}{L}\right)^2 \alpha t} - \left(\frac{4a_1 + 2\beta^2 L}{L \left(\frac{3\pi}{L}\right)^2} \right) e^{-\left(\frac{3\pi}{L}\right)^2 \alpha t}. \quad (28)$$

As mentioned previously, the same truncations can be used to simplify Eqn.22. The steady-state series is negligible, and the transient series can be truncated to one term. Therefore, Eqn. 22 can be simplified to

$$T_b(t) = T_0 + \alpha\beta^2 t + \frac{\beta^2}{2} L^2 + a_1 L + a_0 + \frac{4.04}{kL[J_0(\alpha_1)]^2(p_1^2 + v_1^2)} \left[\frac{q_2 r_0^2}{4} + \frac{q_1 r_0}{3} \right] e^{-(v_1^2 + p_1^2) \alpha t}. \quad (29)$$

IV. Results and Discussion

In the previous section, analytical solutions were derived, and an error analysis was performed to truncate the solutions to a simplified form. In this section, Eqns. 25, 26, 28, and 29 will be validated against slug calorimeter back-face thermal data using optimization in Section IV.A - IV.B. The objective is to find optimal values of the stagnation heat flux and the initial temperature in which the analytical solutions provide a best-fit to the slug thermal data. A least squares approach is used to find optimal variables to produce the best fit using the Generalized Reduced Gradient (GRG) nonlinear optimization method [19, 20]. This approach is an available tool in Excel and requires a good initial guess to ensure an accurate local minimum is returned by the optimization routine. The initial guess for the stagnation heat flux is determined by the ASTM reported value, and in the case of variable (radially varying) heat flux, data acquired from CFD performed in Brune et al. [1] to inform the initial guess of the coefficients in $q(r)$. The guess for the initial temperature is calculated as the average of the slug thermal data points in the first one-tenth of a second, prior to the steady-state portion of the slug thermal response. In Sections IV.C, a summary of the optimization results is given

to make an assessment of the new range of epistemic uncertainty in the stagnation heat flux on the slug probe. In Section IV.D, the aleatory uncertainty is quantified by evaluating temporal variations in the stagnation heat flux in the steady-state portion of the slug thermal response, which is accomplished by using a least-squares slope marching routine. A comparison of the mixed uncertainty, accounting for aleatory and epistemic components, will be presented in Section IV.E and compared to the uncertainty used in Brune et al [1].

A. Analytical 1D Conduction Validation

Using Eqn. 25, T_0 and q_0 are used as optimization variables to minimize the sum of square of the error between the model prediction and slug thermal data points. Figure 15a shows the best fit $T_b(t)$ for the high-enthalpy test condition, which is obtained when $q_0 = 246.7 \text{ W/cm}^2$ and $T_0 = 289.7 \text{ K}$. Figure 15b shows the best fit $T_b(t)$ for the low-enthalpy test condition which is obtained when $q_0 = 60.6 \text{ W/cm}^2$ and $T_0 = 288.5 \text{ K}$. Note the initial guesses used for both conditions are listed in the figure caption and are the same values used for the truncation error analysis in Section III.C. The results demonstrate that Eqn. 25 is a valid and optimized model for predicting the slug thermal response for both enthalpy conditions in the case of constant heat flux across the front face of the slug element.

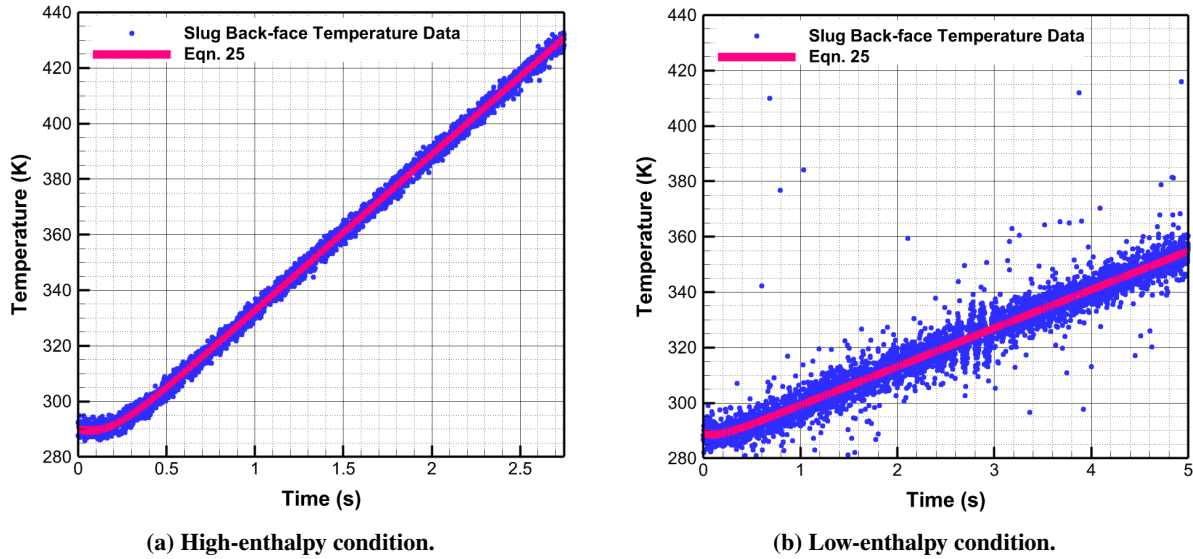


Fig. 15 Comparison of the optimized constant heat flux solution and the slug back-face temperature data with initial guesses: (a) $T_0 = 285.9 \text{ K}$ and $q_0 = 243.1 \text{ W/cm}^2$, (b) $T_0 = 283.2 \text{ K}$ and $q_0 = 56.7 \text{ W/cm}^2$.

Now, assume that the constant heat flux assumption is relaxed, and the heat flux varies radially across the front face of the slug element. As mentioned in Section III.B.2, Eqn. 26 requires designated values for p and q_{avg} in order to evaluate the coefficients of $q(r)$ from Eqns. 7 and 8. The value of q_{avg} is equivalent to the optimized constant heat flux value, q_0 , determined by the optimized model in Eqn. 25. The value of p can be determined by the CFD predictions in Brune et al. [1], which indicates that the heat flux value at $r = r_o$ is approximately 8% higher than the stagnation heat flux predicted value for both high- and low-enthalpy conditions; therefore, $p = 1.08$. For the high-enthalpy condition, evaluating the derived formulas given in Eqns. 7 and 8 result in $q_0 = 237.2 \text{ W/cm}^2$, $q_1 = 0 \text{ W/cm}^3$, and $q_2 = 47.1 \text{ W/cm}^4$. For the low-enthalpy condition, evaluating the derived formulas given in Eqns. 7 and 8 result in $q_0 = 58.2 \text{ W/cm}^2$, $q_1 = 0 \text{ W/cm}^3$, and $q_2 = 11.6 \text{ W/cm}^4$. Note that since q_{avg} equals the optimized q_0 in Eqn. 25, the results shown in Figures 15a and 15b are also applicable to Eqn. 26 for the high- and low-enthalpy conditions.

B. Analytical 2D Conduction Validation

Recall that two possible analytical solutions were derived from two eigenvalue cases in Section III.B.3, as shown by Eqns. 28 and 29. The optimization variables in these analytical models are the initial temperature, T_0 , and the coefficients of the quadratic heat flux equation $q(r)$ i.e. q_2 , q_1 , and q_0 . For this particular optimization problem, the coefficients in $q(r)$ can produce an optimal solution, when left unconstrained, that does not conform fundamentally to an increasing heat flux as the spatial location increases towards the shoulder of the slug element. In an effort to preserve

the shape of the heat flux distribution on the front face of the slug element, consistent with the CFD data in Brune et al.[1], the following constraint is applied to the coefficients in $q(r)$ for some scale factor c :

$$q(r) = cq_2r^2 + cq_1r + cq_0. \quad (30)$$

Therefore, Eqns. 28 and 29 are optimized with respect to the scale factor, c , and the initial temperature, T_0 .

Figures 16a and 16b present the optimized slug back-face thermal response analytical prediction, using Eqn. 29, compared to the slug thermal data for the high- and low-enthalpy test conditions, respectively. This comparison is shown for the case in which the analytical solution adopts a zero-eigenvalue root. The resulting coefficients in the heat flux equation for the high-enthalpy condition are $cq_2 = 44.3 \text{ W/cm}^4$, $cq_1 = -2.4 \text{ W/cm}^3$, and $cq_0 = 237 \text{ W/cm}^2$. For the low-enthalpy condition, the coefficient values are $cq_2 = 10.9 \text{ W/cm}^4$, $cq_1 = -0.53 \text{ W/cm}^3$, and $cq_0 = 58.6 \text{ W/cm}^2$. The results demonstrate that Eqn. 29 is a valid and optimized model, in the case of a zero eigenvalue root, for predicting the slug thermal response for both enthalpy conditions assuming variable heat flux across the front face of the slug element with two-dimensional thermal conduction.

For the case of positive eigenvalues, Figures 17a and 17b present the optimized slug back-face thermal response analytical prediction, using Eqn. 28, compared to the slug thermal data for the high- and low-enthalpy test conditions, respectively. For a true comparison of the positive eigenvalue solution to the zero eigenvalue solution, the T_0 and the $q(r)$ coefficients are set to the aforementioned optimized values in the zero eigenvalue case. A clear distinction can be observed between the two solutions in the first 0.1-0.2 seconds of penetration time since insertion of the slug element into the flow, which is consistent with the differences in the transient terms of the two analytical solutions. Figure 17 indicates a significant deviation from the slug calorimeter data near $t = 0$ and does not follow the behavior of the data for small t , which is primarily due to the exponential term in the transient solution, $e^{-(p_1^2 + v_1^2)at}$. While the transient series is supposed to approach zero as t tends towards infinity, the exponential term forces the transient series to approach zero a short while after $t = 0$ seconds. Furthermore, a large valued expression involving cq_2 and cq_1 is included in the transient series as well, resulting in an ill-posed solution for small adjustments in c that produces significant deviations from the experimental data. Therefore, the positive eigenvalue solution in Eqn. 28 is eliminated as a valid model.

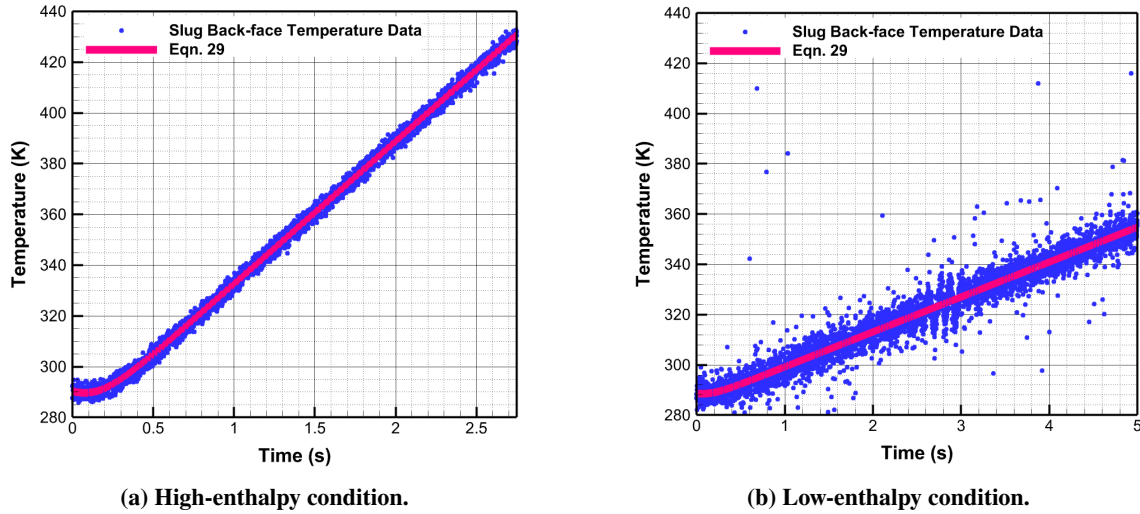


Fig. 16 Comparison of the zero-eigenvalue optimized variable heat flux solution and the slug back-face temperature data with initial guesses: (a) $c = 1.00$, $q_2 = 45.5 \text{ W/cm}^4$, $q_1 = -2.5 \text{ W/cm}^3$, $q_0 = 243.1 \text{ W/cm}^2$, and $T_0 = 285.93 \text{ K}$, (b) $c = 1.00$, $q_2 = 10.5 \text{ W/cm}^4$, $q_1 = -0.51 \text{ W/cm}^3$, $q_0 = 56.7 \text{ W/cm}^2$, and $T_0 = 283.15 \text{ K}$.

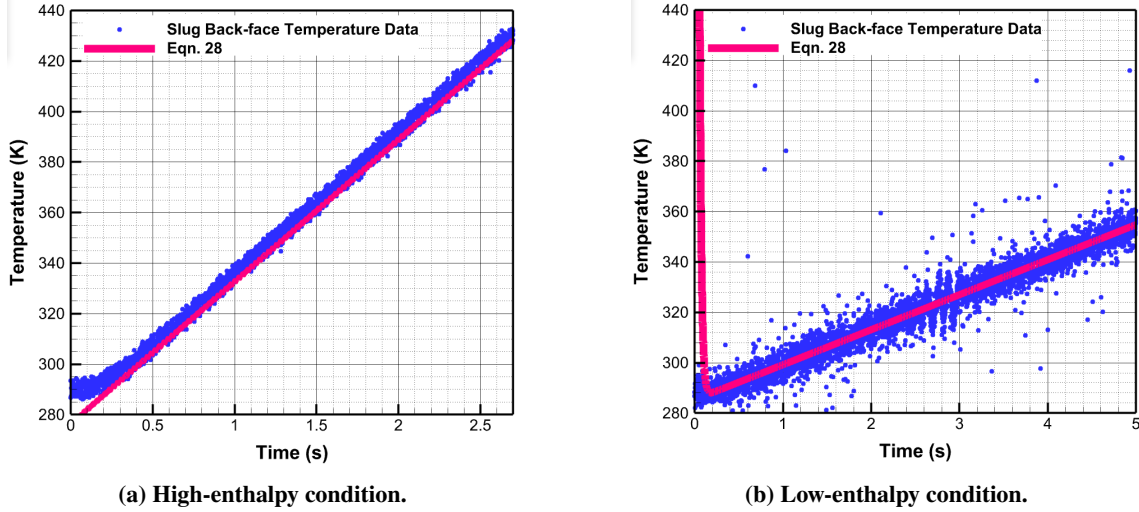


Fig. 17 Comparison of the positive-eigenvalue variable heat flux solution and the slug back-face temperature data with optimized variables in the zero-eigenvalue solution: (a) $c = 0.98$ and $T_0 = 289.6$ K, (b) $c = 1.03$ and $T_0 = 288.6$ K.

C. Evaluation of Deduced Stagnation Heat Flux Epistemic Uncertainty

In the previous subsections, the stagnation heat flux values were evaluated through various slug element non-ideal scenarios, including constant heat flux with one-dimensional conduction, variable heat flux with one-dimensional conduction, and variable heat flux with two-dimensional conduction. Either optimization of the developed analytical solutions or simplified expressions were used to quantify the stagnation heat flux values for these non-ideal slug environments. A summary of the stagnation heat flux values is presented in Table 1 using Eqns. 25, 7, and 29. In the previous subsection, the stagnation heat flux value for Eqn. 28 was not considered because it does not mimic the slug back-face thermal data in the transient phase, prior to the steady-state slope. For comparison, the stagnation heat flux value reported using the ASTM method and the optimal stagnation heat flux value using Eqn. 25 when $f_L = 0$ (no heat losses), which is also presented in [3], has also been provided in the table. In the table, columns are shown for both high- and low-enthalpy conditions that scale the results to the reference ASTM reported deduced stagnation heat flux.

Table 1 Summary of deduced stagnation heat flux values from (1) reported ASTM, (2) optimized analytical solutions from Hightower (no losses), Eqn. 25, and Eqn. 29, and (3) computed analytical formula in Eqn. 7

Case Description	Approach Ref.	Low-enthalpy Condition		High-enthalpy Condition	
		Stag. Heat Flux, q_0 (W/cm ²)	Scale with ASTM Reported	Stag. Heat Flux, q_0 (W/cm ²)	Scale with ASTM Reported
ASTM Reported	[2]	56.7	1.00	243.1	1.00
Constant Heat Flux, 1D conduction, no losses	[3]	60.0	1.06	245.3	1.01
Constant Heat Flux, 1D conduction, 1% loss	Current work	60.6	1.07	246.7	1.02
Variable Heat Flux, 1D conduction, 1% loss	Current work	58.2	1.02	237.2	0.98
Variable Heat Flux, 2D conduction, 1% loss	Current work	58.6	1.03	237.0	0.98

For the low-enthalpy condition, the ASTM reported value is approximately 4.5% lower than the average of the optimized analytical results from this work and Hightower [3]. Notice in the figures shown in Section IV.A IV.B, the slug back-face thermal data for the low-enthalpy condition has more noise compared to the thermal traces for the high-enthalpy condition. Having a significant cloud of noisy data could lead to errors in computing the temperature slope with the ASTM method, which is likely what may have happened in this particular case with the low-enthalpy condition. The approach of using the optimization with the analytical solutions prevents this issue, while the ASTM requires the test engineer to analyze the slug back-face thermal data and be selective in the choice of points to estimate the temperature slope. Otherwise, artificial temperatures slopes could be computed with the ASTM method, thus introducing error in the deduced stagnation heat flux values. In the case of the high-enthalpy condition, the average of

the optimized analytical results from this work and Hightower agree with the ASTM reported value.

Given the scaled reference values in the third and last columns in Table 1, a new stagnation heat flux bias uncertainty range can be determined due to the non-ideal effects that the slug element could experience in a test environment. For both enthalpy conditions, the epistemic uncertainty is evaluated to be $\pm 2\%$ with respect to the average of the results, not including from the ASTM reported value. Recall in Section IV.A, simplified expressions were used to evaluate the $q(r)$ coefficient of the spatial variation in the heat flux across the front face of the slug element. The results show that this simple approach can estimate the stagnation heat flux to within 1% of the more sophisticated zero-eigenvalue analytical solution optimized in Section IV.B. In addition, the simplified approach of assuming variable heat flux with one-dimensional conduction consistently represents at or approximate to the lower bound of the epistemic uncertainty. In a similar fashion, the optimized analytical solution for the constant heat flux case with losses and one-dimensional thermal conduction represents the upper bound of the epistemic uncertainty consistently. Therefore, for any test condition, one could optimize Eqn. 25 and evaluate the expression in Eqn. 7 to determine the epistemic uncertainty due to non-ideal effects of the slug element in the arc-jet environment. From the table, one can also deduce that the primary contribution to the epistemic uncertainty of the deduced stagnation heat flux value is the spatial variation in the heat flux distribution on the front face of the slug element. The spatial variation in the heat flux can vary from one condition to the other due to the nature of the freestream environments in the arc-jet test cabin; fundamental aeroheating theory of flat-face slug calorimeter geometries suggests that the heat flux tends to increase at some degree from the center of the slug element to the shoulder of the calorimeter housing, but the rate of increase is the uncertainty that is covered here for different conditions, in addition to run-to-run variability for a single condition, in the freestream flow that dictates the heat flux distribution on the slug element surface.

D. Evaluation of Deduced Stagnation Heat Flux Aleatory Uncertainty

Now that the epistemic uncertainty has been quantified in the previous subsection, a second component of the uncertainty is addressed here. The aleatory uncertainty is a probabilistic uncertainty that can be used to determine a cumulative density function that represents the temporal variation of the deduced stagnation heat flux over a sample time period. For a given set of back-face slug temperature data, a temperature smoothing routine is applied in the numerical conversion process from temperature to heat flux. Figure 18 shows an example of the temperature smoothing process for a sample of the slug temperature trace data. The temperature smoothing routine uses a marching, or moving, window of a linear least-squares fit. Assume that ten points are used in the linear least-squares fit for this example. The algorithm smooths the first point of the window to point n , which is always the sixth point from the end of the window. The final point in the window is $n + 5$. The window continues to march forward in time. For $n < 5$, the window grows in time until the desired set of points can be obtained from the truncation at the beginning of the temperature data set. Each smoothed temperature point is derived using the formula of a straight line for each point n in the original temperature data set:

$$T_n = m_n t_n + b_n \quad (31)$$

As the routine smooths the data, the stagnation heating rate is determined using the following equation at each point n :

$$q_n = \rho C_p L \left(\frac{T_n - T_{n-1}}{t_n - t_{n-1}} \right) \quad (32)$$

The choice of the number of points in the linear least-squares fit window is arbitrary. An investigation is performed to understand the behavior of the statistics in the heat flux determinations depending on the choice of the number of points in the fit window. For a small number of points in the fit window, a large sample size of heat flux observations can be obtained in the steady-state region of the back-face slug temperature trace. On the other hand, a small sample size of heat flux observations can be obtained if the number of points is too large in the fit window. Therefore, there is a balance of the smoothing process with the number of samples in the heat flux observations. To illustrate this, Figure 19 shows the sample standard deviation dependence on the sample size of the heat flux determinations, which is driven by the selection of the number of fit points. Notice in the figure that a saddle point (or inflection point) is formed as a compromise of the two competing factors, which include noise reduction through linear fit smoothing and statistical convergence with enough sample determinations. For a large sample size with limited number of fit points, there is much noise in the heat flux determination as indicated by the high standard deviation (or variance). As one increases the number of fit points, the statistics begin to converge and become independent of the explicit noise in the temperature data

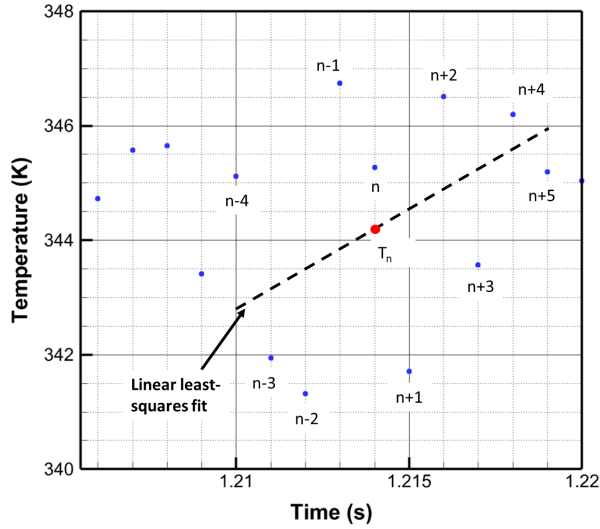


Fig. 18 Example of temperature smoothing process.

through the saddle (or inflection) point of the s-curve in Figure 19. If one increases the number of fit points too much, then the statistical significance of the heat flux observations begins to show degradation and loses the convergence of the sample standard deviation with respect to the sample size of those observations. Therefore, a compromise between the two competing factors is required to obtain a reasonable approximation of the statistics of the heat flux observations through the smoothing routine and heat flux calculation.

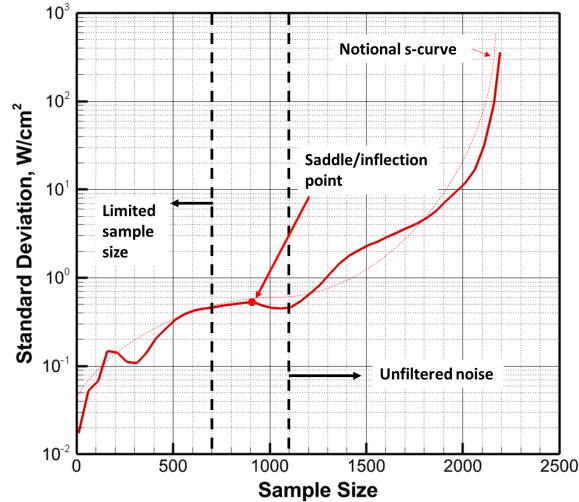


Fig. 19 Dependence of the deduced heat flux sample standard deviation with competing sample size and noise smoothing factors.

As indicated in Figure 19, which is shown for the high-enthalpy case, the optimal standard deviation at the critical saddle/inflection point is determined to be 0.53 W/cm^2 with a corresponding mean of 242.83 W/cm^2 . A similar approach is applied to the low-enthalpy case in determining the inflection point of convergence between smoothing and sample standard deviation. The results indicate an optimal standard deviation of 0.6 W/cm^2 with a sample mean of 59.47 W/cm^2 . A chi-squared goodness of fit test confirms the null hypothesis that the heat flux determinations are sampled from a normal distribution.

E. Summary of Deduced Stagnation Heat Flux Uncertainty

Given the results from the previous two subsections, the evaluation of the epistemic and aleatory uncertainty inform the generation of a probability box plot that represents the mixed uncertainty of the stagnation heat flux on the slug calorimeter. These are informed from the optimized analytical models against the slug back-face thermal data, and the numerical analysis of the slug data to gather temporal statistics across a period of time at the slug element's steady state. Figure 20 compares the current work probability box plot against the intervals used in Brune et al. [1] Historically, the uncertainty in the deduced heat flux from the slug calorimeter temperature data, using the ASTM approach, was $\pm 10\%$. These are indicated in both figures with the red solid lines at the low- and high-enthalpy conditions. From this work, the uncertainty has been reduced to the green solid lines through analysis performed in this section. Adopting a 95% confidence interval to evaluate the new uncertainty in the stagnation heat flux, the value of the upper green cumulative distribution function (CDF) bound at the 97.5% probability level and the value of the lower green CDF bound at the 2.5% probability level are used; the 95% confidence interval values are illustrated in the figures with black circles. For the low-enthalpy case, the 95% confidence interval ranges from 57.05 to 61.81 W/cm^2 , or $\pm 4\%$ from the midpoint of the confidence interval, which is approximate to the average of the results in Table 1. For the high-enthalpy case, the 95% confidence interval is ranges from 235.99 to 247.75 W/cm^2 , or $\pm 2.6\%$ from the midpoint of the confidence interval, which is approximate to the average of the results in Table 1. Note that the uncertainty is higher for the low-enthalpy condition due to the nature of the noise inherent in the slug back-face temperature data compared to the high-enthalpy condition. Compared to the uncertainty applied to the state-of-the-art method in Brune et al. [1], this study shows that the uncertainty in the deduced stagnation heat flux on the slug calorimeter can be reduced by approximately 75% for the high-enthalpy condition and approximately 60% for the low-enthalpy. If there is not a distinction in the noise of the slug temperature traces between the two conditions, the expectation is the uncertainty reduction would follow more closely to the high-enthalpy level of approximately 75%.

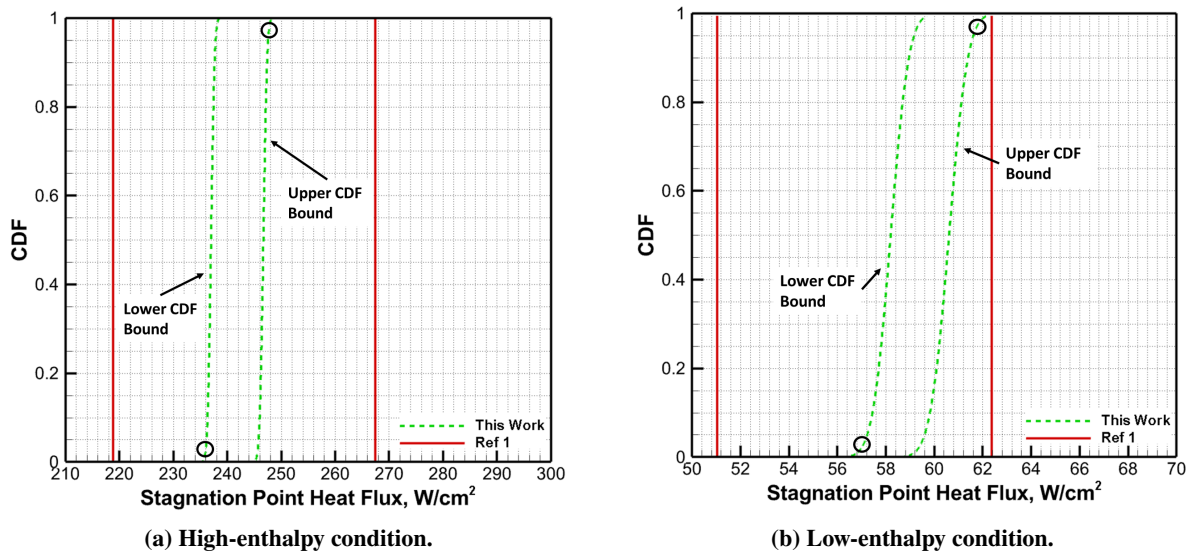


Fig. 20 Comparison of the uncertainty in the deduced stagnation heat flux used in Brune et al. [1] to the uncertainty evaluated in this work.

With the completion of this effort, the work in Brune et al. [1] will be revisited in carrying the new uncertainty in the deduced stagnation heat flux represented by a mixed uncertainty with two components (epistemic bias from an analysis calibration standard and aleatory temporal variation), similar to the stagnation pressure and other arc setpoint parameters. The validation comparison will be conducted between the CFD prediction and facility measurement uncertainty in both stagnation heat flux and pressure metrics. Then, a follow-on calibration of the CFD model will be conducted, using a form of a Bayesian inference approach, to get the model prediction and measurement uncertainty bounds to match with modifications to the CFD model input parameters that warrant adjustment due to lack of analysis or test data. In other words, CFD uncertain parameters with justification simply from expert opinion, or without a reference or analysis to backup the variation of a specific parameter, will be included in the modification process of the model calibration to match prediction and data uncertainty at some threshold of validation error.

V. Conclusion

In summary, an uncertainty analysis is performed on the deduced stagnation heat flux environment of a slug calorimeter for conditions that span the performance envelope of the Hypersonic Materials Environmental Test System facility located at NASA Langley Research Center. Analytical solutions are developed for boundary-value problems on the slug element accounting for non-ideal effects, including spatial variation in the slug heat flux, multi-dimensional thermal conduction, and back-face losses, which departs from the state-of-the-art method derived from the American Society of Testing and Materials standard procedure. Boundary-value problem definitions are informed by preliminary finite element thermal analysis of the slug calorimeter assembly (including both slug and housing) and just the slug element. The analytical solutions are presented in a general sense and in a truncated form from error analysis. Validation through a least squares approach via optimization indicates good agreement between the developed analytical models and available slug back-face thermal data. The compilation of optimization results show that the appropriate epistemic uncertainty of the deduced stagnation heat flux on the slug calorimeter is at most $\pm 2.5\%$ for both a high- and low-enthalpy test condition. In addition, a numerical approach is used to determine the aleatory (probabilistic) uncertainty component in the slug stagnation heat flux by applying a marching least-squares slope routine through the steady-state portion of the slug back-face thermal response. Results indicate a compromise between the number of samples and the filter frequency of slug back-face thermal data points when evaluating the standard deviation of the deduced stagnation heat flux statistics. When combining the mixed uncertainty (both aleatory and epistemic), the interval of uncertainty in the deduced stagnation heat flux is determined to be up to $\pm 4\%$, which is at least 60% reduction from the standard uncertainty used in the state-of-the-art method. Future work includes a feedback loop of new mixed uncertainty shown in this work on the slug calorimeter to update the validation comparison of uncertainty in the computational fluid dynamics model predictions against measurement uncertainty. In addition, model calibration of the computational fluid dynamics model via a Bayesian-inference approach will also be considered to obtain the optimal validation between prediction and measurement uncertainty.

References

- [1] Brune, A. J., West IV, T. K., and White, L. M., "Calibration Probe Uncertainty and Validation for the Hypersonic Material Environmental Test System," *Journal of Thermophysics and Heat Transfer*, Vol. 34, No. 2, 2020, pp. 404–420.
- [2] "Standard Test Method for Measuring Heat-Transfer Rate Using a Thermal Capacitance (Slug) Calorimeter," Tech. rep., ASTM Standard E457-08, 1996.
- [3] Hightower, T. M., Olivares, R. A., and Philippidis, D., "Thermal capacitance (slug) calorimeter theory including heat losses and other decaying processes," *Thermal and Fluids Analysis Workshop (TFAWS) 2008*, 2008.
- [4] Nawaz, A., and Santos, J., "Assessing calorimeter evaluation methods in convective heat flux environments," *10th AIAA/ASME Joint Thermophysics and Heat Transfer Conference*, 2010, p. 4905.
- [5] Dalir, N., "Exact analytical solution for 3d time-dependent heat conduction in a multilayer sphere with heat sources using eigenfunction expansion method," *International scholarly research notices*, Vol. 2014, 2014.
- [6] Jain, P. K., Singh, S., et al., "An exact analytical solution for two-dimensional, unsteady, multilayer heat conduction in spherical coordinates," *International Journal of Heat and Mass Transfer*, Vol. 53, No. 9-10, 2010, pp. 2133–2142.
- [7] Splinter, S., Bey, K., and Gragg, J., "Comparative Measurements of Earth and Martian Entry Environments in the NASA Langley HyMETS Facility," AIAA 2011-1014, 2011. <https://doi.org/10.2514/6.2011-1014>.
- [8] Wiedemann, K., Clark, R., and Sankaran, S., "Emittance, Catalysis, and Dynamic Oxidation of Ti-14AL-21Nb," Tech. rep., NASA TP-2955, Nov. 1989.
- [9] Glass, D., "Oxidation and Emittance Studies of Coated Mo-Re," Tech. rep., NASA CR-201753, Oct. 1997. <https://doi.org/10.1.1.51.2302>.
- [10] Bird, R., Wallace, T., and Sankaran, S., "Development of Protective Coatings for High-Temperature Metallic Materials," *Journal of Spacecraft and Rockets*, Vol. 41, No. 2, 2004, pp. 213–220. <https://doi.org/10.2514/1.9191>.
- [11] Calomino, A., Bruce, W., Gage, P., Horn, D., Mastaler, M., Rigali, D., Robey, J., Voss, L., Wahlberg, J., and Williams, C., "Evaluation of the NASA Arc-Jet Capabilities to Support Mission Requirements," Tech. rep., NASA SP-2010-577, Nov. 1989.
- [12] American Society for Testing Materials (ASTM), ., "Standard Test Method for Measuring Heat-Transfer Rate Using a Thermal Capacitance (Slug) Calorimeter," Tech. rep., ASTM Standard E457-96, 1996.

- [13] Nawaz, A., and Santos, J., “Assessing Calorimeter Evaluation Methods in Convective and Radiative Heat Flux Environment,” AIAA 2010-4905, 2010. <https://doi.org/10.2514/6.2010-4905>.
- [14] Brune, A., Bruce, W., Glass, D., and Splinter, S., “Computational Simulations of the NASA Langley HyMETS Arc-Jet Facility,” Tech. rep., NASA NF1676L-28439, 2017.
- [15] Simon, N. J., Drexler, E. S., and Reed, R. P., “Properties of Copper and Copper Alloys at Cryogenic Temperature,” Tech. rep., NIST Monograph 177, Feb. 1992.
- [16] White, G. K., and Collocott, S. J., “Heat Capacity of Reference Materials: Cu and W,” *Journal of Physical and Chemical Reference Data*, Vol. 13, No. 4, 1984, pp. 1251–1258.
- [17] Incropera, F. P., and DeWitt, D. P., *Fundamentals of Heat and Mass Transfer, 3rd ed.*, John Wiley and Sons, New York, 1990.
- [18] COMSOL, “COMSOL Multiphysics User’s Guide, v5.5,” Tech. rep., COMSOL/CM-020005, Oct. 2019.
- [19] Lasdon, L. S., Waren, A. D., Jain, A., and Ratner, M., “Design and Testing of a Generalized Reduced Gradient Code for Nonlinear Programming,” *ACM Trans. Math. Softw.*, Vol. 4, No. 1, 1978, p. 34–50. <https://doi.org/10.1145/355769.355773>.
- [20] Lasdon, L., Fox, R., and Ratner, M., “Nonlinear Optimization Using the Generalized Reduced Gradient Method,” *Revue Française d’Automatique, Informatique, Recherche Opérationnelle. Série Verte*, Vol. 8, 1973, p. 63. <https://doi.org/10.1051/ro/197408V300731>.

Appendix

In Section III.B.1 - III.B.3, multiple analytical solutions were presented and claimed to satisfy their initial respective boundary-value problems. The purpose of the appendix is to provide a detailed description of how Eqns. 4 and 16 were derived, and to mathematically prove, the claim of satisfying their boundary value-problems. It should be noted that the process of deriving and verifying Eqn. 15 is similar to the work shown in Section B of the Appendix.

A. Derivation and Verification of the Constant Heat Flux Solution

As noted in Section III.B.1 , Eqn. 4 satisfies the governing equation $T_{xx} = \frac{1}{\alpha}T_t$ (Eqn. 2) whose initial and boundary conditions were given in Eqn. 3: $T(x, 0) = T_0, T_x(0, t) = -\frac{q_0}{k}, T_x(L, t) = -\frac{f_L q_0}{k}$. Assume the solution is of the form

$$T(x, t) = (\text{steady state}) + (\text{transient}) = v(x, t) + w(x, t). \quad (33)$$

For the steady-state solution, use the separation of variables $v(x, t) = f(x) + g(t)$. This choice creates a nonhomogeneous initial-boundary value problem as follows:

$$v_{xx} = \frac{1}{\alpha}v_t \quad (34)$$

$$v_x(0, t) = f'(0) = -\frac{q_0}{k} \quad (35)$$

$$v_x(L, t) = f'(L) = -\frac{f_L q_0}{k} \quad (36)$$

$$v(x, 0) = g(0) = T_0. \quad (37)$$

Plugging in the required partial derivatives into Eqn. 34 gives the equivalence $f''(x) = \frac{1}{\alpha}g'(t)$. This equation only holds if $f''(x) = \frac{1}{\alpha}g'(t) = \lambda$ for some constant λ , which gives two ordinary differential equations, $f''(x) = \lambda$ and $g'(t) = \alpha\lambda$. Standard integration gives $f(x) = \frac{\lambda}{2}x^2 + c_1x + c_2$ and $g(t) = \alpha\lambda t + c_3$ where each c_i is a constant.

The values of λ, c_1 and c_3 can be found using the boundary and initial conditions:

$$f'(0) = \lambda(0) + c_1 = -\frac{q_0}{k} \quad \longrightarrow \quad c_1 = -\frac{q_0}{k} \quad (38)$$

$$f'(L) = \lambda L + c_1 = -\frac{f_L q_0}{k} \quad \longrightarrow \quad \lambda = -\frac{c_1}{L} - \frac{f_L q_0}{kL} = \frac{q_0}{kL} - \frac{f_L q_0}{kL} = \frac{(1 - f_L)q_0}{kL} \quad (39)$$

$$g(0) = \alpha\lambda(0) + c_3 = T_0 \quad \longrightarrow \quad c_3 = T_0 \quad (40)$$

With substitution, $v(x, t) = \frac{(1-f_L)q_0}{2kL}x^2 - \frac{q_0}{k}x + c_2 + \frac{(1-f_L)\alpha q_0}{kL}t + T_0$. Using the energy balance equation,

$$\frac{1}{L} \int_0^L v(x, t) dx = T_0 + \frac{(1-f_L)\alpha q_0 t}{kL}, \quad (41)$$

it can be shown $c_2 = \frac{(2+f_L)q_0L}{6k}$. Therefore, the steady-state solution is

$$v(x, t) = f(x) + g(t) = \frac{(1-f_L)q_0}{2kL}x^2 - \frac{q_0}{k}x + \frac{(2+f_L)q_0L}{6k} + \frac{(1-f_L)\alpha q_0 t}{kL} + T_0. \quad (42)$$

For $T(x, t) = (\text{steady state}) + (\text{transient}) = v(x, t) + w(x, t)$ to satisfy its initial-boundary value problem, $w(x, t) \neq 0$ must satisfy the following initial-value problem:

$$w_{xx} = \frac{1}{\alpha} w_t \quad (43)$$

$$w_x(0, t) = 0 \quad (44)$$

$$w_x(L, t) = 0 \quad (45)$$

$$w(x, 0) = T_0 - v(x, 0) = -f(x). \quad (46)$$

To find a nonzero solution to Eqn. 43, use the separation of variables $w(x, t) = \phi(x)\theta(t)$. Taking partial derivatives and plugging into our governing equation gives the separable equation $\phi''(x)\theta(t) = \frac{1}{\alpha}\phi(x)\theta'(t)$. With some rearranging, the separable equation becomes $\frac{\phi''(x)}{\phi(x)} = \frac{\theta'(t)}{\alpha\theta(t)}$ which only holds if $\frac{\phi''(x)}{\phi(x)} = \frac{\theta'(t)}{\alpha\theta(t)} = -d^2$ for some nonzero constant d . This results in two ordinary differential equations, $\phi'' + d^2\phi = 0$ and $\theta' + \alpha d^2\theta = 0$.

The first equation can be solved using the characteristic equation $\sigma^2 + d^2 = 0$. The roots of this equation are $\sigma = \pm di$ which correspond to solutions $\phi_1(x) = \cos(dx)$ and $\phi_2(x) = \sin(dx)$. Therefore, the general solution is $\phi(x) = A \cos(dx) + B \sin(dx)$ where A and B are constants.

The second differential equation can be solved by the integrating factor,

$$\mu(t) = e^{\int \alpha d^2 dt} = e^{\alpha d^2 t}. \quad (47)$$

Multiplying by $\mu(t)$, gives the equation $e^{\alpha d^2 t} \theta' + \alpha d^2 e^{\alpha d^2 t} \theta = 0$ of which the left-hand side is the derivative of the product $\mu\theta$. Therefore,

$$\theta(t) = \frac{1}{\mu} \int 0 dt = C e^{-\alpha d^2 t} \quad (48)$$

for some constant C .

Equation 44 gives the relation $\phi'(0)\theta(t) = 0$ which must hold for every t . Thus, $\phi'(0) = 0$ implying $-Ad \sin(0) + Bd \cos(0) = 0$ or simply $Bd = 0$. Since $d \neq 0$, $B = 0$. Similarly, Eqn. 49 gives the relation $\phi'(L)\theta(t) = 0$ which again must hold for every t . Therefore, $\phi'(L) = 0$. That is, $-Ad \sin(dL) + Bd \cos(dL) = 0$ or simply $-Ad \sin(dL) = 0$. Note $A \neq 0$, for if both A and B are zero then $w(x, t) = 0$. It must be the case that $\sin(dL) = 0$ since $d \neq 0$. Hence, $dL = n\pi$ for positive integers n . In particular, $d_n = \frac{n\pi}{L}$ where n is any positive integer. The family of solutions obtained from these computations are $\phi_n(x) = A_n \cos\left(\frac{n\pi x}{L}\right)$ and $\theta_n(t) = C_n e^{-\alpha\left(\frac{n\pi}{L}\right)^2 t}$. Putting this together we have the transient solution

$$w(x, t) = \sum_{n=1}^{\infty} a_n e^{-\alpha\left(\frac{n\pi}{L}\right)^2 t} \cos\left(\frac{n\pi x}{L}\right) \quad (49)$$

where $a_n = A_n C_n$.

Equations 46 and 49 gives

$$\sum_{n=1}^{\infty} a_n \cos\left(\frac{n\pi x}{L}\right) = -f(x) = -\frac{(1-f_L)q_0}{2kL}x^2 + \frac{q_0}{k}x - \frac{(2+f_L)q_0L}{6k}. \quad (50)$$

The cosine Fourier series gives a_n to be

$$a_n = \frac{2}{L} \int_0^L -f(x) \cos\left(\frac{n\pi}{L}\right) dx = \frac{2q_0L[(-1)^n f_L - 1]}{k\pi^2 n^2}. \quad (51)$$

Therefore, the general solution for $T(x, t)$ is

$$T(x, t) = T_0 + \frac{(1-f_L)q_0}{2kL}x^2 - \frac{q_0}{k}x + \frac{(2+f_L)q_0L}{6k} + \frac{(1-f_L)\alpha q_0 t}{kL} + \frac{2q_0L}{k\pi^2} \sum_{n=1}^{\infty} \left[\frac{(-1)^n f_L - 1}{n^2} \right] e^{-\alpha\left(\frac{n\pi}{L}\right)^2 t} \cos\left(\frac{n\pi x}{L}\right) \quad (52)$$

as claimed.

While the details of the derivation of $T(x, t)$ have been provided, it still needs to be verified that $T(x, t)$ satisfies the initial-boundary problem. The left-hand side of the governing equation is

$$T_{xx} = \frac{(1-f_L)q_0}{kL} - \frac{2q_0}{kL} \sum_{n=1}^{\infty} [(-1)^n f_L - 1] e^{-\alpha\left(\frac{n\pi}{L}\right)^2 t} \cos\left(\frac{n\pi x}{L}\right) \quad (53)$$

while the right-hand side is

$$\begin{aligned} \frac{1}{\alpha} T_t &= \frac{1}{\alpha} \left[\frac{(1-f_L)\alpha q_0}{kL} - \frac{2\alpha q_0}{kL} \sum_{n=1}^{\infty} [(-1)^n f_L - 1] e^{-\alpha\left(\frac{n\pi}{L}\right)^2 t} \cos\left(\frac{n\pi x}{L}\right) \right] \\ &= \frac{(1-f_L)q_0}{kL} - \frac{2q_0}{kL} \sum_{n=1}^{\infty} [(-1)^n f_L - 1] e^{-\alpha\left(\frac{n\pi}{L}\right)^2 t} \cos\left(\frac{n\pi x}{L}\right). \end{aligned} \quad (54)$$

Since the left and right-hand sides agree, $T(x, t)$ satisfies the partial differential equation.

The last item that needs to be verified is $T(x, t)$ satisfies the initial and boundary conditions:

$$T_x(0, t) = v_x(0, t) + w_x(0, t) = -\frac{q_0}{k} + 0 = -\frac{q_0}{k} \quad (55)$$

$$T_x(L, t) = v_x(L, t) + w_x(L, t) = -\frac{f_L q_0}{k} + 0 = -\frac{f_L q_0}{k} \quad (56)$$

$$T(x, 0) = v(x, 0) + w(x, 0) = f(x) + T_0 - f(x) = T_0. \quad (57)$$

Therefore, $T(x, t)$ satisfies the one-dimensional initial-boundary value problem.

In Section III.B.1, it was claimed the solution satisfying the two-dimensional heat equation,

$$T_{xx} + T_{rr} = \frac{1}{\alpha} T_t - \frac{1}{r} T_r, \quad (58)$$

with boundary and initial conditions

$$\begin{aligned} T_r(0, x, t) = 0 \quad T_x(r, 0, t) = -\frac{q_0}{k} \quad T(r, x, 0) = T_0. \\ T_r(r_0, x, t) = 0 \quad T_x(r, L, t) = -\frac{f_L q_0}{k} \end{aligned} \quad (59)$$

is $T(x, t)$ (Eqn. 4). The first step in showing this is to assume the solution is of the form $T(r, x, t) = (\text{steady state}) + (\text{transient}) = v(r, x, t) + w(r, x, t)$. From here, the method for deriving $T(r, x, t)$ is identical to the one used to derive Eqn. 16 in Section B of the Appendix. However, one difference to this solution is the computation of the coefficients in the steady-state series. Both A_n and B_n are zero since their Fourier series computations involve the integral, $\int_0^{r_0} r J_0(p_n r) dr = \frac{(r_0)^2 J_1(\alpha_n)}{\alpha_n} = 0$. Recall α_n is a root of J_1 for all positive integers n . With these calculations, the choice of separation of variables for the steady-state solution,

$$v(r, x, t) = f(r, x) + g(t) = [\text{homogeneous solution} + \text{particular solution}] + g(t) = f_H(r, x) + f_P(r, x) + g(t) \quad (60)$$

results in $f_H(r, x) = 0$ which reduces $f(r, x)$ to $f_p(r, x)$. As $f_p(r, x)$ is a polynomial in only the variable x , the steady-state solution, $v(r, x, t)$, is independent of r . For the transient solution, the separation of variables $w(r, x, t) = R(r)X(x)\tau(t)$ coupled with the initial condition, $T(r, x, 0) = -f_p(r, x)$, eventually leads to $w(r, x, t) = 0$. Since a nonzero transient solution is desired, it is concluded that $w(r, x, t)$ must be independent of r , which leads to $w(r, x, t) = w(x, t)$ from Eqn. 4. Since $v(r, x, t) = v(x, t)$ and $w(r, x, t) = w(x, t)$ from Eqn. 4, $T(r, x, t) = T(x, t)$ as claimed.

To show $T(x, t)$ satisfies the two-dimensional heat equation, take appropriate partial derivatives of $T(x, t)$ and plug into the two-dimensional governing equation. Note T_{xx} and T_t were computed in Eqns. 53 and 54 and $T_r(r, x, t) = T_r(x, t) = 0$ for all values of r since $T(x, t)$ is independent of r . Plugging in the respective derivatives into the governing equation yields the partial differential equation, $T_{xx} = \frac{1}{\alpha}T_t$. By previous work, $T(x, t)$ satisfies this differential equation.

For the boundary conditions, it is clear $T_r(0, x, t) = 0 = T_r(r_0, x, t)$ for all x, t . Furthermore, equations 55 - 57 show $T_x(r, 0, t) = T_x(0, t) = -\frac{q_0}{k}$, $T_x(r, L, t) = T_x(L, t) = -\frac{f_L q_0}{k}$, and $T(r, x, 0) = T(x, 0) = T_0$ as desired. In conclusion, $T(x, t)$ is a solution to both the one-dimensional and two-dimensional initial-boundary value problems with constant heat flux.

B. Derivation and Verification of the Variable Heat Flux Solution (Zero-Eigenvalue Root)

For the derivation of Eqn. 16, assume again the general solution is of the form

$$T(x, r, t) = v(r, x, t) + w(r, x, t) = (\text{steady state}) + (\text{transient}). \quad (61)$$

Similar to the constant heat flux solution, this choice gives two initial boundary-value problems:

$$\begin{aligned} v_{xx} + v_{rr} &= \frac{1}{\alpha}v_t - \frac{1}{r}v_r & w_{xx} + w_{rr} &= \frac{1}{\alpha}w_t - \frac{1}{r}w_r \\ v_r(0, x, t) &= 0 & w_r(0, x, t) &= 0 \\ v_r(r_0, x, t) &= 0 & w_r(r_0, x, t) &= 0 \\ v_x(r, 0, t) &= -\frac{q(r)}{k} & w_x(r, 0, t) &= 0 \\ v_x(r, L, t) &= -\frac{f_L q(r)}{k} & w_x(r, L, t) &= 0 \\ v(r, x, 0) &= T_0 & w(r, x, 0) &= T_0 - v(r, x, 0) \end{aligned} \quad (62)$$

As previously stated, the separation of variables choice for the steady-state solution is $v(r, x, t) = f(r, x) + g(t)$. Thus, the boundary and initial conditions become

$$f_r(0, x) = 0, \quad f_r(r_0, x) = 0, \quad f_x(r, 0) = -\frac{q(r)}{k}, \quad f_x(r, L) = -\frac{f_L q(r)}{k}, \quad g(0) = T_0. \quad (63)$$

Plugging into Eqn. 58 and separating the variables gives $f_{xx} + f_{rr} + \frac{1}{r}f_r = \frac{1}{\alpha}g_t = \beta^2$ where β is the separation constant. This results in two differential equations, $g_t = \alpha\beta^2$ and $f_{xx} + f_{rr} + \frac{1}{r}f_r = \beta^2$.

Integrating the first equation with respect to t gives $g(t) = \alpha\beta^2 t + c_1$. Applying the initial condition $g(0) = T_0$, implies $c_1 = T_0$. Therefore, $g(t) = \alpha\beta^2 t + T_0$.

For the second nonhomogeneous differential equation, the general solution must be of the form $f(r, x) = f_h(r, x) + f_p(r, x)$ where $f_h(r, x)$ satisfies $f_{xx} + f_{rr} + \frac{1}{r}f_r = 0$ and $f_p(r, x)$ is any particular solution satisfying $f_{xx} + f_{rr} + \frac{1}{r}f_r = \beta^2$. Assume $f_h(r, x) = F(r)G(x)$. This will transform the differential equation into $G''F + GF'' + \frac{1}{r}GF' = 0$ or equivalently $\frac{G''}{G} + \frac{F''}{F} + \frac{1}{r}\frac{F'}{F} = 0$. Separating the variables, gives

$$\frac{G''}{G} = -\frac{F''}{F} - \frac{1}{r}\frac{F'}{F} = p^2 \quad (64)$$

where p is some real constant. The two resulting differential equations are $G'' - p^2G = 0$ and $F'' + \frac{1}{r}F' + p^2F = 0$.

The first ODE has characteristic equation $\sigma^2 - p^2 = 0$ whose roots are $\sigma = \pm p$. Therefore, $G(x) = A \cosh(px) + B \sin(px)$. The second ODE can be rewritten in the form $r^2F'' + rF' + p^2r^2F = 0$ and has general solution $F(r) = CJ_0(pr) + DY_0(pr)$ where J_0 is the Bessel function of the first kind of order zero and Y_0 is the Bessel function of the second kind of order zero. In order to make $F(r)$ defined at $r = 0$, D must be zero. Therefore, the general solution simplifies to $F(r) = CJ_0(pr)$. In conclusion,

$$f_h(r, x) = [A \cosh(px) + B \sinh(px)]J_0(pr). \quad (65)$$

The method of undetermined coefficients suggests $f_p(r, x)$ is of the form $f_p(r, x) = a_2x^2 + a_1x + a_0$. Taking derivatives and plugging into the nonhomogeneous equation will give $a_2 = \frac{\beta^2}{2}$ while a_1 and a_0 can be any real numbers. Therefore, the general solution for $f(r, x) = [A \cosh(px) + B \sinh(px)]J_0(pr) + \frac{\beta^2}{2}x^2 + a_1x + a_0$.

With the results from above, the general solution for the steady-state solution is $v(r, x, t) = [A \cosh(px) + B \sinh(px)]J_0(pr) + \frac{\beta^2}{2}x^2 + a_1x + a_0 + \alpha\beta^2t + T_0$. However, the boundary conditions of the steady-state initial-boundary value problem still need to be satisfied. Note $v_r(r, x) = f_r(r, x) = -p[A \cosh(px) + B \sinh(px)]J_1(pr)$, so $v_r(0, x) = f_r(0, x) = 0$ since $J_1(0) = 0$. Also, for $v_r(r_0, x) = f_r(r_0, x) = -p[A \cosh(px) + B \sinh(px)]J_1(pr_0) = 0$ for all x , then pr_0 must be a root of J_1 . Therefore, we define $p_n = \frac{\alpha_n}{r_0}$ where α_n ($n = 1, 2, 3, \dots$) is any positive root of J_1 . Thus, the new form of $f(r, x)$ becomes

$$f(r, x) = \sum_{n=1}^{\infty} [A_n \cosh(p_n x) + B_n \sinh(p_n x)] J_0(p_n r) + \frac{\beta^2}{2} x^2 + a_1 x + a_0. \quad (66)$$

The partial of $f(r, x)$ with respect to x is $f_x(r, x) = \sum_{n=1}^{\infty} p_n [A_n \sinh(p_n x) + B_n \cosh(p_n x)] J_0(p_n r) + \beta^2 x + a_1$. The boundary condition $f_x(r, 0) = -\frac{q(r)}{k}$ gives the relation

$$-\frac{q(r)}{k} = a_1 + \sum_{n=1}^{\infty} p_n B_n J_0(p_n r). \quad (67)$$

With some rearrangement, this relation is equivalent to

$$-\frac{q(r)}{k} - a_1 = \sum_{n=1}^{\infty} p_n B_n J_0(p_n r). \quad (68)$$

Using a Fourier series for J_0 , we obtain

$$p_n B_n = \frac{-\int_0^{r_0} \left(\frac{q(r)}{k} + a_1 \right) r J_0(p_n r) dr}{\int_0^{r_0} r J_0^2(p_n r) dr} = \frac{-2}{k(r_0)^2 [J_0(\alpha_n)]^2} \sum_{m=0}^{\infty} \frac{(-1)^m (\alpha_n)^{2m}}{2^{2m} [m!]^2} \left[\frac{q_2(r_0)^4}{2m+4} + \frac{q_1(r_0)^3}{2m+3} \right]. \quad (69)$$

With some algebra and reindexing, B_n simplifies to

$$B_n = \frac{-2}{k p_n [J_0(\alpha_n)]^2} \sum_{m=1}^{\infty} \frac{(-1)^{m-1} (\alpha_n)^{2m-2}}{2^{2m-2} [(m-1)!]^2} \left[\frac{q_2(r_0)^2}{2m+2} + \frac{q_1 r_0}{2m+1} \right]. \quad (70)$$

The final boundary condition $f_x(r, L) = -\frac{f_L q(r)}{k}$, gives the relation

$$-\frac{f_L q(r)}{k} = \beta^2 L + a_1 + \sum_{n=1}^{\infty} p_n [A_n \sinh(p_n L) + B_n \cosh(p_n L)] J_0(p_n r) \quad (71)$$

which is equivalent to

$$-\frac{f_L q(r)}{k} - \beta^2 L - a_1 = \sum_{n=1}^{\infty} p_n [A_n \sinh(p_n L) + B_n \cosh(p_n L)] J_0(p_n r). \quad (72)$$

Again, using a Fourier series associated to J_0 , gives

$$p_n [A_n \sin(p_n L) + B_n \cosh(p_n L)] = \frac{\int_0^{r_0} \left[-\frac{f_L q(r)}{k} - \beta^2 L - a_1 \right] r J_0(p_n r) dr}{\int_0^{r_0} r J_0^2(p_n r) dr}. \quad (73)$$

In particular,

$$\begin{aligned}
A_n &= -\frac{B_n \cosh(p_n L)}{\sinh(p_n L)} - \frac{2}{(r_0)^2 p_n \sinh(p_n L) [J_0(\alpha_n)]^2} \int_0^{r_0} \left[\frac{f_L q(r)}{k} + \beta^2 L + a_1 \right] r J_0(p_n r) dr \\
&= -\frac{B_n \cosh(p_n L)}{\sinh(p_n L)} - \frac{2}{(r_0)^2 p_n \sinh(p_n L) [J_0(\alpha_n)]^2} \int_0^{r_0} \frac{f_L}{k} (q_2 r^2 + q_1 r) r J_0(p_n r) + \left(\frac{f_L q_0}{k} + \beta^2 L + a_1 \right) r J_0(p_n r) dr \\
&= -\frac{B_n \cosh(p_n L)}{\sinh(p_n L)} - \frac{2}{(r_0)^2 p_n \sinh(p_n L) [J_0(\alpha_n)]^2} \left(\frac{f_L}{k} \sum_{m=0}^{\infty} \frac{(-1)^m (\alpha_n)^{2m}}{2^{2m} [m!]^2} \left[\frac{q_2 (r_0)^4}{2m+4} + \frac{q_1 (r_0)^3}{2m+3} \right] \right) \\
&\quad - \frac{2}{(r_0)^2 p_n \sinh(p_n L) [J_0(\alpha_n)]^2} \left(\frac{f_L q_0}{k} + \beta^2 L + a_1 \right) \frac{(r_0)^2 J_1(\alpha_n)}{\alpha_n} \\
&= -\frac{B_n \cosh(p_n L)}{\sinh(p_n L)} + \frac{f_L}{\sinh(p_n L)} \left[\frac{-2}{k p_n [J_0(\alpha_n)]^2} \sum_{m=0}^{\infty} \frac{(-1)^m (\alpha_n)^{2m}}{2^{2m} [m!]^2} \left[\frac{q_2 (r_0)^2}{2m+4} + \frac{q_1 r_0}{2m+3} \right] \right] + 0 \\
&= -\frac{B_n \cosh(p_n L)}{\sinh(p_n L)} + \frac{f_L B_n}{\sinh(p_n L)} \\
&= B_n \left[\frac{f_L - \cosh(p_n L)}{\sinh(p_n L)} \right].
\end{aligned} \tag{74}$$

Combining all the above work gives the steady-state solution,

$$v(r, x, t) = T_0 + \alpha \beta^2 t + \frac{\beta^2}{2} x^2 + a_1 x + a_0 + \sum_{n=1}^{\infty} [A_n \cosh(p_n x) + B_n \sinh(p_n x)] J_0(p_n r) \tag{75}$$

$$= T_0 + \alpha \beta^2 t + \frac{\beta^2}{2} x^2 + a_1 x + a_0 + \sum_{n=1}^{\infty} B_n \left[\left(\frac{f_L - \cosh(p_n L)}{\sinh(p_n L)} \right) \cosh(p_n x) + \sinh(p_n x) \right] J_0(p_n r). \tag{76}$$

Note β^2 , a_1 , and a_0 are constants in the steady-state solution that are yet to be determined. Since the value of a_1 and a_0 can be any real number, these are chosen to coincide with the coefficients in model 9 :

$$a_1 = -\frac{q_{avg}}{k} \quad \text{and} \quad a_0 = \frac{(2 + f_L) q_{avg} L}{6k}. \tag{77}$$

β^2 was computed by solving

$$\beta^2 = \frac{\int_0^{2\pi} \int_0^{r_0} r(1 - f_L) q(r) dr d\theta}{k L \pi (r_0)^2} = \frac{(1 - f_L) q_{avg}}{k L}. \tag{78}$$

For the transient solution, use the method of separation of variables and assume $w(r, x, t) = R(r)X(x)\tau(t)$. Taking appropriate derivatives and plugging into the differential equation, gives the separable equation

$$RX''\tau + R''X\tau = \frac{1}{\alpha} RX\tau' - \frac{1}{r} R'X\tau. \tag{79}$$

Dividing each term by $RX\tau$ along with some rearranging gives

$$\frac{X''}{X} + \frac{R''}{R} + \frac{1}{r} \frac{R'}{R} = \frac{1}{\alpha} \frac{\tau'}{\tau} = -\lambda^2 \tag{80}$$

where $-\lambda^2$ is the separation constant. This gives the two differential equations, $\tau' + \alpha \lambda^2 \tau = 0$ and $\frac{X''}{X} + \frac{R''}{R} + \frac{1}{r} \frac{R'}{R} = -\lambda^2$. The second equation can be separated further in the following way

$$\frac{X''}{X} = -\frac{R''}{R} - \frac{1}{r} \frac{R'}{R} - \lambda^2 = -v^2 \tag{81}$$

where $-v^2$ is some nonzero constant. Thus, there are three ordinary differential equations that need to be solved:

$$1) \tau' + \alpha\lambda^2\tau = 0$$

$$2) X'' + v^2X = 0$$

$$3) r^2R'' + rR' + (\lambda^2 - v^2)r^2R = 0.$$

The first equation has solution $\tau(t) = Ce^{-\lambda^2\alpha t}$ which can be derived using the integrating factor, $e^{\lambda^2\alpha t}$. The second and third differential equations can be solved with techniques used in the derivation of $f_h(r, x)$ in the steady solution. The solutions from these methods are $X(x) = A \cos(vx) + B \sin(vx)$ and $R(r) = DJ_0(sr)$ where $s^2 = \lambda^2 - v^2$.

Using the boundary conditions, gives

$$w_r(0, x, t) = R'(0) = -sDJ_1(s \cdot 0) = 0 \quad (82)$$

$$w_r(r_0, x, t) = R'(r_0) = -sDJ_1(s \cdot r_0) = 0 \quad (83)$$

$$w_x(r, 0, t) = X'(0) = -vA \sin(v \cdot 0) + vB \cos(v \cdot 0) = vB = 0 \quad (84)$$

$$w_x(r, L, t) = X'(L) = -vA \sin(vL) + vB \cos(vL) = 0 \quad (85)$$

Notice the first boundary condition is satisfied since zero is a root of J_1 . The second boundary condition holds as long as sr_0 is a root of J_1 . For Eqn. 23, the value of s was chosen to be zero implying all eigenvalues are zero. The third boundary condition implies $B = 0$ since v is assumed to be nonzero. Last, the fourth boundary condition gives $-vA \sin(vL) = 0$ after substitution. Since neither A nor v is zero, it must be $\sin(vL) = 0$. Therefore, $vL = z\pi$ for some integer z . Thus, the eigenvalues are $v_z = \frac{z\pi}{L}$ for all positive integers z .

The solutions to the three differential equations above are

$$1) \tau(t) = C_z e^{-v_z^2 \alpha t}$$

$$2) X(x) = A_z \cos(v_z x)$$

$$3) R(r) = DJ_0(0 \cdot r) = D$$

and each satisfy their respective initial-value problem. Therefore, the transient solution is

$$w(r, x, t) = \sum_{z=1}^{\infty} E_z e^{-v_z^2 \alpha t} \cos(v_z x) \quad (86)$$

where $E_z = A_z C_z D$.

The initial condition $w(r, x, 0) = T_0 - v(r, x, 0)$ is equivalent to $w(r, x, 0) = \sum_{z=1}^{\infty} E_z \cos(v_z x) = -f(r, x)$. A cosine Fourier series can be used to find the value of E_z ,

$$E_z = \frac{2}{L} \int_0^L -f(r, x) \cos(v_z x) dx = \frac{(-1)^{z+1} (2\beta^2 L + 2a_1) + 2a_1}{Lv_z^2} - \frac{2}{L} \sum_{n=1}^{\infty} \frac{p_n B_n [(-1)^z f_L - 1]}{p_n^2 + v_z^2}. \quad (87)$$

Substituting in B_n and simplifying gives

$$E_z = \frac{(-1)^{z+1} (2\beta^2 L + 2a_1) + 2a_1}{Lv_z^2} + \sum_{n=1}^{\infty} \sum_{m=1}^{\infty} \frac{[(-1)^z f_L - 1]}{kL(p_n^2 + v_z^2)[J_0(\alpha_n)]^2} \left[\frac{(-1)^{m-1} (\alpha_n)^{2m-2}}{2^{2m-4} [(m-1)!]^2} \right] \left[\frac{q_2(r_0)^2}{2m+2} + \frac{q_1 r_0}{2m+1} \right]. \quad (88)$$

Now that the steady-state and transient solutions have been derived, the solution to the two-dimensional boundary value problem is

$$T(r, x, t) = v(r, x, t) + w(r, x, t) \quad (89)$$

$$= T_0 + \alpha\beta^2 t + \frac{\beta^2}{2} x^2 + a_1 x + a_0 + \sum_{n=1}^{\infty} [A_n \cosh(p_n x) + B_n \sinh(p_n x)] J_0(p_n r) + \sum_{z=1}^{\infty} E_z e^{-v_z^2 \alpha t} \cos(v_z x) \quad (90)$$

To ensure the computations in deriving $T(r, x, t)$ are correct, it is necessary to verify $T(r, x, t)$ satisfies the initial-boundary value problem. To start this process, first take the appropriate partial derivatives of $T(r, x, t)$:

$$T_x = \beta^2 x + a_1 + \sum_{n=1}^{\infty} p_n [A_n \sinh(p_n x) + B_n \cosh(p_n x)] J_0(p_n r) - \sum_{z=1}^{\infty} v_z E_z e^{-v_z^2 \alpha t} \sin(v_z x) \quad (91)$$

$$T_{xx} = \beta^2 + \sum_{n=1}^{\infty} p_n^2 [A_n \cosh(p_n x) + B_n \sinh(p_n x)] J_0(p_n r) - \sum_{z=1}^{\infty} v_z^2 E_z e^{-v_z^2 \alpha t} \cos(v_z x) \quad (92)$$

$$T_r = - \sum_{n=1}^{\infty} p_n [A_n \cosh(p_n x) + B_n \sinh(p_n x)] J_1(p_n r) \quad (93)$$

$$T_{rr} = - \sum_{n=1}^{\infty} p_n^2 [A_n \cosh(p_n x) + B_n \sinh(p_n x)] J_1'(p_n r) \quad (94)$$

$$T_t = \alpha \beta^2 - \sum_{z=1}^{\infty} v_z^2 \alpha E_z e^{-v_z^2 \alpha t} \cos(v_z x) \quad (95)$$

Plugging into the governing equation, $T_{xx} + T_{rr} = \frac{1}{\alpha} T_t - \frac{1}{r} T_r$, the left-hand side simplifies to

$$\beta^2 + \sum_{n=1}^{\infty} p_n^2 [A_n \cosh(p_n x) + B_n \sinh(p_n x)] J_0(p_n r) - \sum_{z=1}^{\infty} v_z^2 E_z e^{-v_z^2 \alpha t} \cos(v_z x) - \sum_{n=1}^{\infty} p_n^2 [A_n \cosh(p_n x) + B_n \sinh(p_n x)] J_1'(p_n r) \quad (96)$$

$$= \beta^2 - \sum_{z=1}^{\infty} v_z^2 E_z e^{-v_z^2 \alpha t} \cos(v_z x) + \sum_{n=1}^{\infty} p_n^2 [A_n \cosh(p_n x) + B_n \sinh(p_n x)] [J_0(p_n r) - J_1'(p_n r)] \quad (97)$$

In order to show the right-hand side is equal to the left-hand side of the governing equation, the following identity will be needed

$$J_0(p_n r) - J_1'(p_n r) = \frac{1}{p_n r} J_1(p_n r). \quad (98)$$

The work below provides the details on why this identity holds.

$$J_0(p_n r) - J_1'(p_n r) = \sum_{m=0}^{\infty} \frac{(-1)^m (p_n r)^{2m}}{2^{2m} [m!]^2} - \sum_{m=0}^{\infty} \frac{(-1)^m (2m+1) (p_n r)^{2m}}{2^{2m+1} [m!(m+1)!]} = \sum_{m=0}^{\infty} \frac{(-1)^m (p_n r)^{2m}}{2^{2m+1} [m!(m+1)!]} [2(m+1) - (2m+1)] \quad (99)$$

$$= \sum_{m=0}^{\infty} \frac{(-1)^m (p_n r)^{2m}}{2^{2m+1} [m!(m+1)!]} [2m+2 - 2m-1] = \sum_{m=0}^{\infty} \frac{(-1)^m (p_n r)^{2m}}{2^{2m+1} [m!(m+1)!]} \quad (100)$$

$$= \sum_{m=0}^{\infty} \frac{(-1)^m (p_n r)^{2m}}{2^{2m+1} [m!(m+1)!]} \left(\frac{p_n r}{p_n r} \right) = \frac{1}{p_n r} \sum_{m=0}^{\infty} \frac{(-1)^m (p_n r)^{2m+1}}{2^{2m+1} [m!(m+1)!]} = \frac{1}{p_n r} J_1(p_n r) \quad (101)$$

Now substituting in the right hand side of the governing equation gives

$$\frac{1}{\alpha} \left[\alpha \beta^2 - \sum_{z=1}^{\infty} v_z^2 \alpha E_z e^{-v_z^2 \alpha t} \cos(v_z x) \right] - \frac{1}{r} \left[- \sum_{n=1}^{\infty} p_n [A_n \cosh(p_n x) + B_n \sinh(p_n x)] J_1(p_n r) \right] \quad (102)$$

$$= \beta^2 - \sum_{z=1}^{\infty} v_z^2 E_z e^{-v_z^2 \alpha t} \cos(v_z x) + \frac{1}{r} \sum_{n=1}^{\infty} p_n [A_n \cosh(p_n x) + B_n \sinh(p_n x)] J_1(p_n r) \quad (103)$$

$$= \beta^2 - \sum_{z=1}^{\infty} v_z^2 E_z e^{-v_z^2 \alpha t} \cos(v_z x) + \sum_{n=1}^{\infty} p_n^2 [A_n \cosh(p_n x) + B_n \sinh(p_n x)] \left(\frac{1}{r p_n} \right) J_1(p_n r) \quad (104)$$

$$= \beta^2 - \sum_{z=1}^{\infty} v_z^2 E_z e^{-v_z^2 \alpha t} \cos(v_z x) + \sum_{n=1}^{\infty} p_n^2 [A_n \cosh(p_n x) + B_n \sinh(p_n x)] [J_0(p_n r) - J_1'(p_n r)] \quad (105)$$

Therefore, $T(r, x, t)$ is a solution to the two-dimensional partial differential equation.

Using the steady-state and transient initial-value problems, the initial and boundary conditions for $T(r, x, t)$ are easily checked:

$$T_r(0, x, t) = v_r(0, x, t) + w_r(0, x, t) = 0 + 0 = 0 \quad (106)$$

$$T_r(r_0, x, t) = v_r(r_0, x, t) + w_r(r_0, x, t) = 0 + 0 = 0 \quad (107)$$

$$T_x(r, 0, t) = v_x(r, 0, t) + w_x(r, 0, t) = -\frac{q(r)}{k} + 0 = -\frac{q(r)}{k} \quad (108)$$

$$T_x(r, L, t) = v_x(r, L, t) + w_x(r, L, t) = -\frac{f_L q(r)}{k} + 0 = -\frac{f_L q(r)}{k} \quad (109)$$

$$T(r, x, 0) = v(r, x, 0) + w(r, x, 0) = v(r, x, 0) + T_0 - v(r, x, 0) = T_0. \quad (110)$$

Thus, $T(r, x, t)$ satisfies the two-dimensional boundary value problem as desired.